Polyphased Inversions of an Intracontinental Rift: Case Study of the Marrakech High Atlas, Morocco

R. Lepretre, Y. Missenard, J. Barbarand, C. Gautheron, I. Jouvie, O. Saddiqi

AGU PUBLICATIONS

Tectonics

RESEARCH ARTICLE
10.1002/2017TC004693

Key Points:
- First large-scale integrated low-temperature thermochronology data sets across the High Atlas
- Late Cretaceous-Cenozoic inversion of the High Atlas shows four stages of deformation, focused within the former rift
- Postrift inversion is facilitated through sedimentary thermal blanket, structural inheritance, and lithospheric thinning

Supporting Information:
- Supporting Information S1

Correspondence to:
R. Leprêtre,
remi.lep@gmail.com

Citation:
Leprêtre, R., Missenard, Y., Barbarand, J., Gautheron, C., Jouvie, I., & Saddiqi, O. (2018). Polyphased inversions of an intracontinental rift: Case study of the Marrakech High Atlas, Morocco. *Tectonics*, *37*, 818–841. https://doi.org/10.1002/2017TC004693

Received 14 JUN 2017
Accepted 11 FEB 2018
Accepted article online 16 FEB 2018
Published online 7 MAR 2018

Polyphased Inversions of an Intracontinental Rift: Case Study of the Marrakech High Atlas, Morocco

R. Leprêtre[1,2], Y. Missenard[1], J. Barbarand[1], C. Gautheron[1], I. Jouvie[1,3], and O. Saddiqi[4]

[1]GEOPS, Université Paris-Sud, CNRS Université Paris-Saclay, Orsay, France, [2]Département Géosciences et Environnement, Université de Cergy-Pontoise, Cergy-Pontoise, France, [3]IGE, Université Joseph Fourier, Grenoble, France, [4]Faculté des Sciences, Université Hassan II, Casablanca, Morocco

Abstract The High and Middle Atlas intraplate belts in Morocco correspond to Mesozoic rifted basins inverted during the Cenozoic during Africa/Eurasia convergence. The Marrakech High Atlas lies at a key location between Atlantic and Tethyan influences during the Mesozoic rifting phase but represents today high reliefs. Age and style of deformation and the mechanisms underlying the Cenozoic inversion are nevertheless still debated. To solve this issue, we produced new low-temperature thermochronology data (fission track and [U-Th]/He on apatite). Two cross sections were investigated in the western and eastern Marrakech High Atlas. Results of inverse modeling allow recognizing five cooling events attributed to erosion since Early Jurassic. Apart from a first erosional event from Middle/Late Jurassic to Early Cretaceous, four stages can be related to the convergence processes between Africa and Europe since the Late Cretaceous. Our data and thermal modeling results suggest that the inversion processes are guided at first order by the fault network inherited from the rifting episodes. The sedimentary cover and the Neogene lithospheric thinning produced a significant thermal weakening that facilitated the inversion of this ancient rift. Our data show that the Marrakech High Atlas has been behaving as a giant pop-up since the beginning of Cenozoic inversion stages.

1. Introduction

In intraplate settings, inverted structures are thought to result from a strong mechanical coupling between a collision zone and its associated forelands (Ziegler et al., 1995). These inverted structures are often localized at the locus of former inherited extensional features (e.g., Central Australia (Hand & Sandiford, 1999; High Atlas, Mattauer et al., 1977)). Inversion processes are directly related with the lithosphere strength, which depends on the crust and lithospheric mantle compositions and thicknesses, the thermal state of the lithosphere, the amount of deformation and its rate (Kusznir & Park, 1987; Sandiford, 1999; Stephenson et al., 2009), and the preexistence of structural inheritance weaknesses (e.g., Bonini et al., 2012; Coward, 1996).

The Middle and High Atlas in Morocco are intraplate Cenozoic compressional belts, resulting from the basin inversion of two branches of a Triassic-Early Jurassic rift (Beauchamp et al., 1999; Mattauer et al., 1977) (Figure 1). Their present-day foreland basins are poorly developed, preventing a clear understanding of the deformation agenda. The belt exhibits a very narrow elevated zone with elevations reaching 4,000 m in the Marrakech High Atlas (MHA). It raises question about the mechanisms that can produce such high reliefs. Indeed, it is well known that the Middle Atlas and the MHA do not have a thickened crustal root and that the mean topography is compensated at depth by a thinned lithosphere (Ayarza et al., 2014; Fullea et al., 2010; Jimenez-Munt et al., 2011; Missenard et al., 2006; Teixell et al., 2005).

To discuss the mechanisms of basin inversion and its timing in the MHA, we carried out a low-temperature thermochronology (LTT) study along two cross sections of the western and the eastern MHA (Figures 2 and 3). We used LTT on apatite, with fission track and (U-Th)/He dating (AFT and AHe, respectively), combined with thermal modeling (Gallagher, 2012). It allows reconstructing the thermal evolution of the first 3–4 km in the crust (Flowers et al., 2009; Gallagher et al., 1998; Gautheron et al., 2009). A wealth of data exists for the MHA (Balestrieri et al., 2009; Ghorbal, 2009; Missenard et al., 2008), but no consensus could be found regarding its precise timing of deformation. We produced 5 new AFT and 16 new AHe data sets in the western MHA and the southern foreland (Askaoun-Siroua plateau). With a more regional consideration than the previous

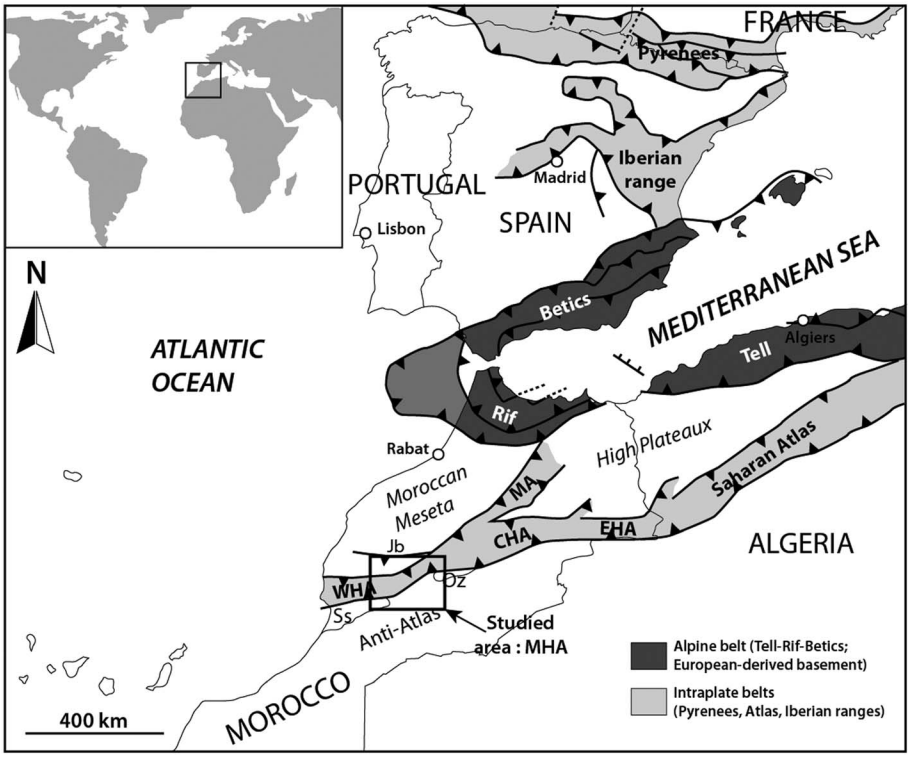

Figure 1. General location of the studied area. WHA: Western High Atlas; MHA: Marrakech High Atlas; CHA: Central High Atlas; EHA: Eastern High Atlas; SA: Saharan High Atlas; Ss: Souss Basin: Oz: Ouarzazate Basin; Jb: Jebilet front.

studies, we have reconsidered the whole existing data set in order to reconstruct the evolution of the MHA along two 60 and 90 km long cross sections. Based on our results, we propose a new deformation agenda for the western MHA and eastern MHA. Our results allow discussing their tectonic styles and reappraising of the position of the main thrust fronts.

2. Geological Setting

The MHA represents a key domain between the Western High Atlas and the Central High Atlas. It displays the highest elevations of the belt, at the former boundary between the Atlantic and Tethysian domain. Moreover, this area shows a significant change in the structural orientation of the chain from N70–90° in the west to N40–60° in the eastern MHA (Figure 1). In addition, the MHA is bounded by poorly developed foreland basins, that is, the Late Cretaceous-Cenozoic discontinuous Souss-Ouarzazate foreland basin in the southwest and the Haouz plain in the north.

2.1. Basement of the MHA

The MHA is constituted by a Precambrian basement covered to the west by a Paleozoic cover intruded by some plutons (Figure 2). The Paleozoic domain displays Variscan deformations due to the collision between Laurentia and Gondwana (Michard et al., 2010). This Paleozoic domain lies between the Tizin'Test Fault Zone to the south and the Haouz plain to the north. It is separated by the Tizin'Test Fault Zone and its northeastern continuity from the southeastern Ouzellarh salient, consisting mainly of Precambrian rocks belonging to the Anti-Atlas range and crosscut by the South Atlas Front (SAF; Figure 2).

The Paleozoic deformations are mainly controlled by the Tizin'Test Fault Zone (Petit, 1976; Proust et al., 1977; Qarbous et al., 2003). The Paleozoic orientations are oblique to the Mesozoic structures (Michard et al., 2010) authorizing discrimination between inherited and newly formed structures (Domènech et al., 2015). The Paleozoic domain is intruded by few plutons (Figure 2a), mostly Permian in age (Gasquet et al., 1992; Mrini et al., 1992), postdating the main Late Carboniferous collisional events.

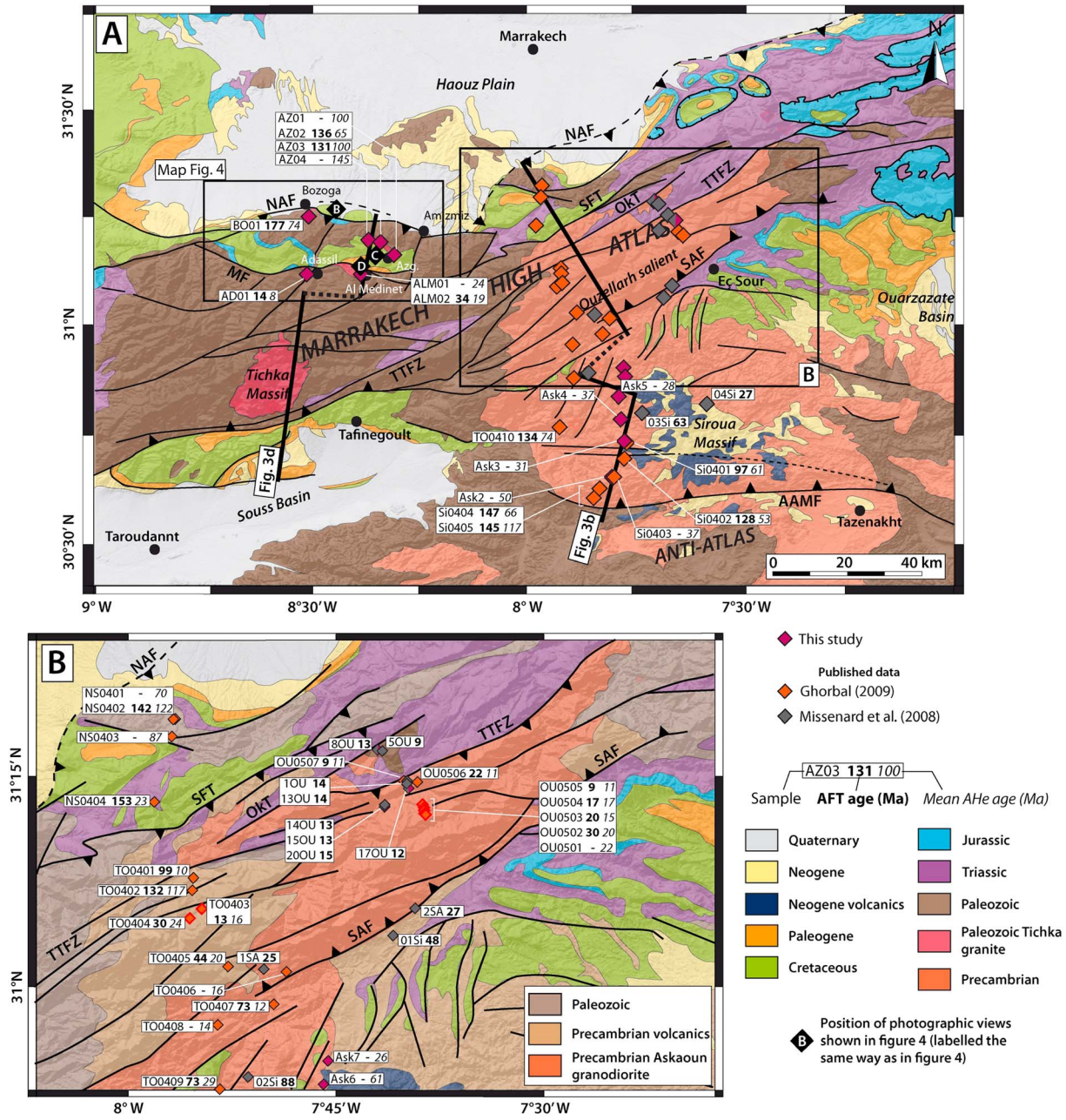

Figure 2. Geological map of the MHA. (a) Geological map of the MHA, with location of the samples and focus in Figure 2b. Colors indicate the origin of the data. AFT and mean AHe ages are given for each sample. The black diamonds with a letter inside indicate the position of photographical views shown in Figure 4. NAF: North Atlas Front; MF: Medinet Fault; TTFZ: Tizin'Test Fault Zone; SAF: South Atlas Front; OkT: Oukaimeden Thrust; SFT: Sidi Fars Thrust; AAMF: Anti-Atlas Major Fault; Azg.:Azegour. (b) Geological map focusing on the eastern MHA with location of the rest of the samples. Same legend as the map in Figure 2a except for the Paleozoic and the Precambrian, the latter being further differentiated. The diamonds with a red contour show the samples corrected for elevation in the modeling stage (see Figure 6 and Tables 1 and 2).

2.2. Postrift Deformations in the MHA

In the High Atlas belt, the thrust fronts are often partially reactivating the old boundaries of the Triassic-Liassic rift (Beauchamp et al., 1999; Domènech et al., 2015; Mattauer et al., 1977). They have been mainly described within the deformed forelands and the Paleozoic domain. Missenard et al. (2007) described the various décollement levels that lead in characteristic deformations around the MHA. These décollement levels induce shallow deformations using Mesozoic weak levels, later crosscut by activation of deeper Paleozoic décollement levels. One early study investigated the deformation in the northern part of the western MHA

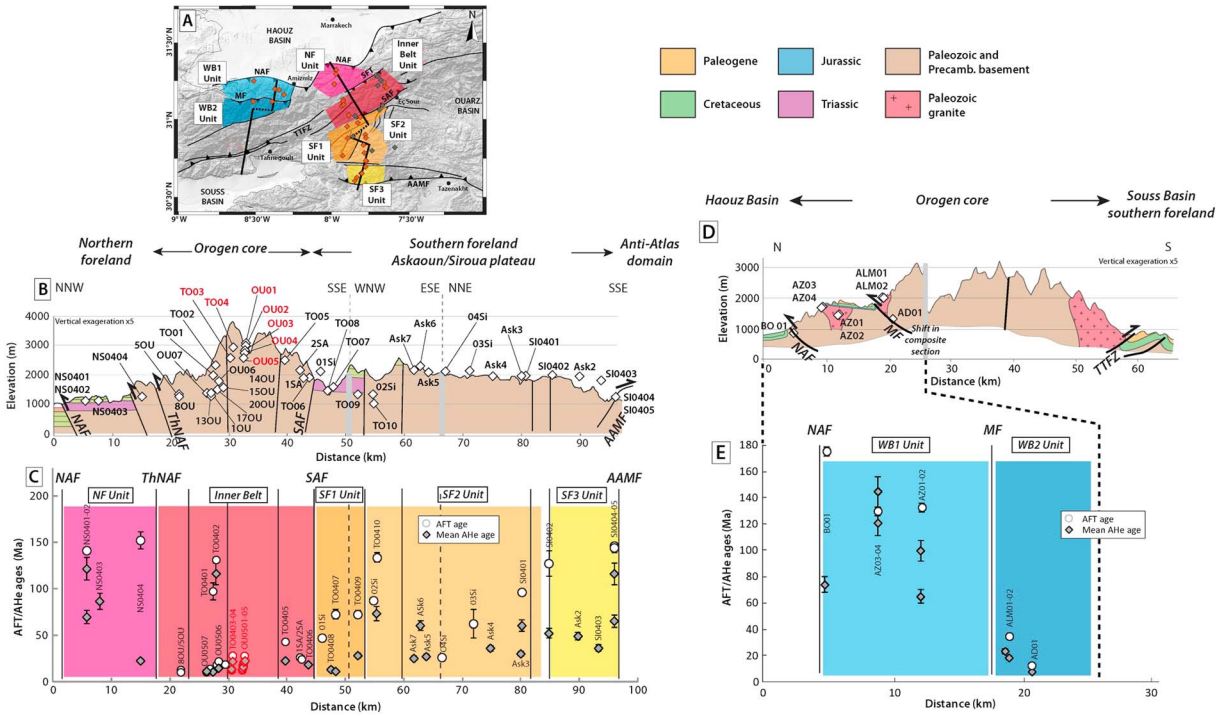

Figure 3. Presentation of the two LTT cross sections. (a) DEM map of the studied area. Colored areas differentiate the different structural units defined in the text. (b, d) Position of all samples, projected along the eastern and western MHA cross sections, respectively, with the position of the major faults. Red names for samples in the inner belt identify the samples corrected for elevation. For faults, same legend as in Figure 2. (c, e) AFT and AHe ages projected along the two cross sections. Red labels also identify the samples corrected for elevation in the inner belt. Background colors indicate the structural segmentation given in Figure 3a.

showing sparse evidences linked to compressive deformations as early as in the Late Cretaceous (Froitzheim et al., 1988).

We describe from west to east the preserved sedimentary cover and the deformation affecting the area. On the northern flank of the western MHA, Jurassic-Cretaceous plateaus are incorporated to the inner belt and lay unconformably on the Paleozoic basement (Froitzheim et al., 1988) (Figures 3 and 4). No Triassic deposit exists in this area. The plateaus show a southward dip of few degrees, are almost undeformed, and stand at elevations higher than 1,000 m (Figures 4c and 4d). They also preserve patches of marine Eocene deposits. To the south, these plateaus are thrust by the Paleozoic basement through the north verging Medinet Fault (Froitzheim et al., 1988) (Figures 4a and 4d). Missenard et al. (2007) described the northern front, separating the Miocene-Quaternary Haouz Basin from the MHA. Few evidences from outcrops and subsurface data allow determining clear location and geometry of the northern front (Missenard et al., 2007) (Figures 2a and 4b). Yet a reverse basement fault is required to explain the present-day elevations of the plateaus (Figures 2a, 4a, and 4b). The NAF near Amizmiz nonetheless shows only moderate inversion since the major front is considered to lie northward, in the Jebilet massif, where an inverse south dipping fault shows an important vertical throw of ~3 km (Hafid et al., 2006). Northeastward, the Tizin'Test Fault zone keeps extending northeastward and branches with the Oukaimeden Thrust (Figure 2a) but the NAF lies north of it, after Missenard et al. (2007) (Figure 1b, NAF).

On the southern side of the western MHA, the SAF is a steep reverse fault reactivating the Tizin'Test Fault zone (El Mustaphi et al., 1997; Frizon de Lamotte et al., 2000). Eastward, the SAF is a fault formed during the Mesozoic that crosscuts the Ouzellarh salient with a NE-SW orientation (Figure 2a). Here the SAF represents an inherited rifting fault with kilometric vertical throw during the Cenozoic (Missenard et al., 2007).

At last, within the (mostly Precambrian) MHA, after a deformation mainly due to dip slip during the Triassic rifting phase (Domènech et al., 2015; Proust et al., 1977; Qarbous et al., 2003), possible basement folding, minor reactivation of former normal faults and mostly newly formed faults characterize moderate Cenozoic inversion (Domènech et al., 2015; Laville & Piqué, 1991; Missenard et al., 2007).

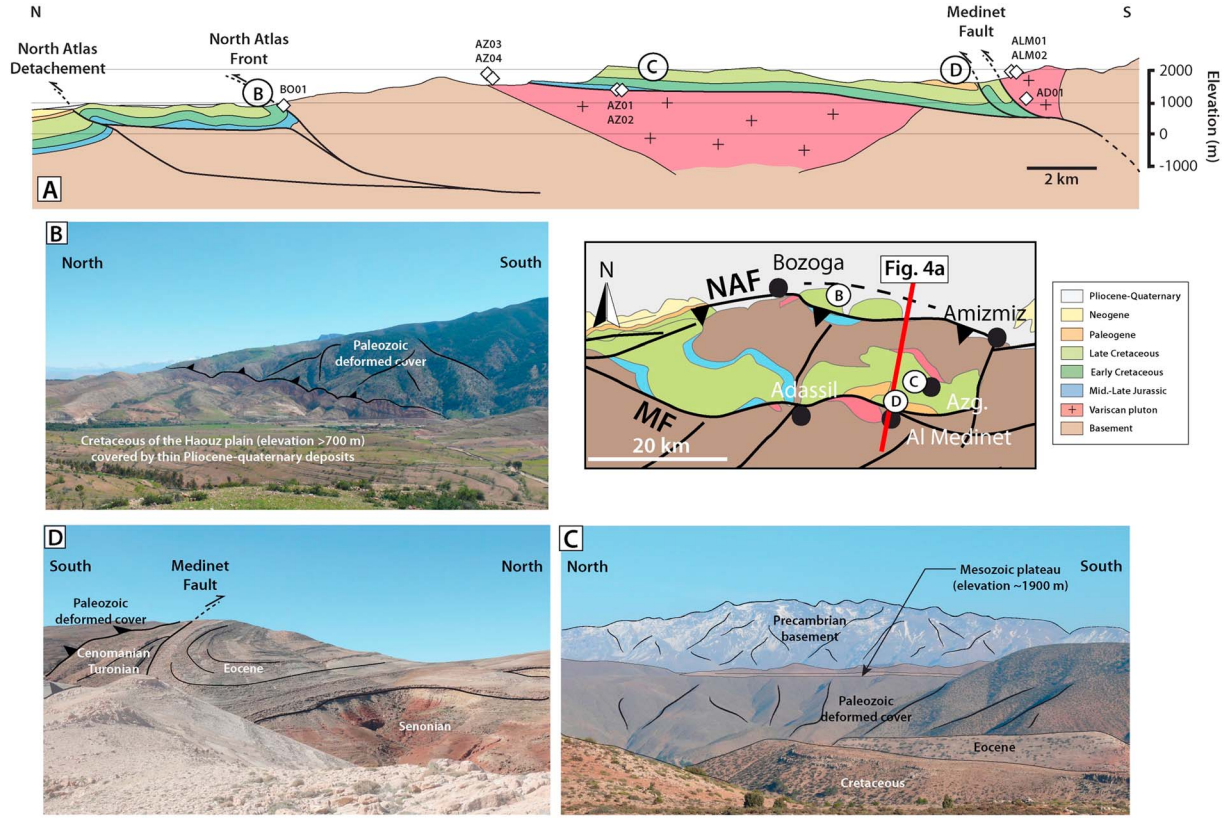

Figure 4. Geometry of the Jurassic-Cretaceous plateau in the northern western MHA. (a) Cross section of the Amizmiz Plateau with main faults and location of the different photos (Figures 4b–4d). Cross section is adapted from the fieldwork by Fekkak et al. (2018). It details the section of Figure 3d, on a neighbor trace, and is slightly extended in the north compared to the trace of Figure 3d. Samples from the western MHA are positioned, projected along the section. (b) Northern front of the western MHA, east of Bozoga (Figure 2a). (c) View on the Mesozoic formations as unconformable plateau on the Paleozoic basement. (d) Thrust and folded Mesozoic-Cenozoic formations on the footwall of the Medinet Fault. It is worth to notice that the Eocene formations are slightly unconformable on the "Senonian" (which represents the Coniancian-Maastrichtian serie) showing the first Late Cretaceous event (see text).

2.3. Deformation Agenda

The timing of deformation is not clearly constrained due to the poorly developed and discontinuous Souss-Ouarzazate Late Cretaceous-Cenozoic syntectonic basin, south of the MHA (Beauchamp et al., 1999; El Harfi et al., 2001; Mustaphi et al., 1997) (Figure 2a). The earliest events are recorded during the Late Cretaceous (Froitzheim et al., 1988) and recognized through LTT by Domènech, Teixell, and Stockli (2016). For the Cenozoic, proposed scenarios can be split between (1) a single Oligocene-Neogene protracted deformation phase scenario (Beauchamp et al., 1999; Teson & Teixell, 2008) and (2) scenarios proposing a polyphased deformation history (El Harfi et al., 2001; Frizon de Lamotte et al., 2000; Görler et al., 1988) with two major events intervening in the middle-late Eocene and in the Pliocene-Quaternary, in addition with a Miocene event, specific to the eastern MHA (Leprêtre, Missenard, Saint-Bezar, et al., 2015).

3. Methodology

3.1. LTT Sampling and Method

Along the eastern MHA cross section, eight new samples were dated with the AHe method (OK and ASK samples; Figures 2 and 3). Three new fission track length data sets were obtained from samples of Missenard et al. (2008). The western MHA cross section encompasses eight new samples with five new AFT and eight new AHe data sets (Figures 2a and 3).

Separation and selection of apatite crystals were done following classical procedures (e.g., Leprêtre, Missenard, Saint-Bezar, et al., 2015). For AFT analysis, we used the external detector and the central age

methods (Galbraith & Laslett, 1993; Gleadow & Duddy, 1981) with a personal zeta (R. L.) of 368 ± 10 (with CN5 glass dosimeters and Durango/Fish Canyon apatite standards) (Hurford, 1990). For AHe dating, ejection factors and sphere equivalent radius were determined after Ketcham et al. (2011). He, U, Th, and Sm content determination is described in Gautheron et al. (2013). The analysis was calibrated using internal and external age standards (i.e., 16.8 ± 1.1 Ma from Kraml et al., 2006, and 31.4 ± 0.2 Ma from McDowell et al., 2005). The error on the AHe age at 1σ is estimated to be a maximum of 8% reflecting uncertainty in the ejection factor (FT) correction and standard dispersion. AFT and AHe data sets are reported in Tables 1 and 2.

3.2. Thermal Modeling

For thermal modelings of all LTT data, we used the QTQt software (Gallagher, 2012). Procedures regarding thermal modeling for complex data sets can be found in Gallagher (2012) for the technical aspects, in Leprêtre, Missenard, Barbarand, et al. (2015) for few examples, and in the supporting information (Text S1).

For the eastern MHA transect (Figure 3b), we carried out a joint inversion of the LTT data mimicking a pseudovertical profile, that is, without taking into account the lateral offset between samples (Figure 2). We combined 16 samples, having either a complete AFT data set (age + lengths) or AHe ages, or both data sets, including 3 and 13 samples from the studies of Missenard et al. (2008) and Ghorbal (2009), respectively. We did not use the AFT ages from the study of Balestrieri et al. (2009) for being similar to those from Missenard et al. (2008). The samples are vertically distributed over ~1,500 m (Figure 5).

For the western MHA transect (Figure 3d, we mostly used individual thermal modelings with QTQt or joint inversion for samples belonging to the same pluton at different elevations. Stratigraphical data have been used as constraints for modeling (Figure 5).

4. Results

We describe the LTT data sets for each subregion combining published data and our new one. We then present the thermal modeling results, separating the western MHA and the eastern MHA. For each cross section, the area is subdivided into structural units, bounded by the main faults, which are known from literature (Figures 2 and 5a). Furthermore, based on the LTT record, a refinement of this subdivision allows recognizing the role of other minor faults. It is then used to separate structural units with different LTT records, described hereafter from north to south.

4.1. Eastern MHA Transect

The LTT ages along the eastern transect suggest a separation between this inner belt and the forelands that display significantly older AFT and AHe ages (Figures 3b and 3c and Tables 1 and 2). The "forelands" are here considered literally as the areas in front of the main deforming zone, corresponding to the inner belt. We include in the description the data from Missenard et al. (2008) and Ghorbal (2009).

4.1.1. Northern Foreland (Figures 2b, 3b, and 3c)

AFT ages are 142 ± 2 and 153 ± 9 Ma (Table 1). MTLs are 12.1 ± 0.3 and 13 ± 0.2 μm, and TLDs are unimodal with narrow spread (Ghorbal, 2009). Dpar values are 1.6 ± 0.2 and 1.7 ± 0.2 μm.

Single-grain AHe ages vary between 14 ± 1 and 141 ± 9 Ma (Table 2). To sum up, samples are getting younger as they are closer to the NAF2 (14 ± 1 to 38 ± 2 Ma; NS0404), compared to samples close to the NAF1 (52 ± 4 to 141 ± 9 Ma; NS0401-03).

4.1.2. Inner Belt

Nineteen AFT ages range from 9 ± 1 to 44 ± 2 Ma in addition with two significantly older ages of 98 ± 9 and 132 ± 3 Ma (Figures 2b and 3c and Table 1; TO0401 and TO0402 samples), discussed later and not used for modeling. Samples display mean track lengths (MTLs) between 11.3 ± 0.3 and 14.1 ± 0.2 μm. Except for one, all MTLs are longer than 12.5 μm (Table 1) with a relative spread of the track length distribution (TLD; standard deviation between 0.6 and 2.1 μm; Table 1 and Figure S1 for 8OU, 14OU, and 20OU samples) (Ghorbal, 2009). Dpar ranges between 1.6 ± 0.2 and 2.3 ± 0.3 μm. A positive relationship exists between AFT ages and elevation (Figure 6a). In detail, some AFT ages stay out of the general trend, by a 500–600 m elevation difference (Figures 2b and 6). These samples belong to the same structural unit, and we interpret this as the result of recent fault activity along these unit boundaries that cannot be detected by LTT (Figure 2b). Thus, the present-day elevation of these samples has been corrected to match the general

AGU Tectonics

10.1002/2017TC004693

Table 1
AFT Results

	Sample *Rock type*	Elevation (m)	ρ_s (10^6 tr/cm^2)	ρ_i (10^6 tr/cm^2)	ρ_d (10^6 tr/cm^2)	Central age (ma) ± 1σ	$P(\chi^2)$ %	U (ppm)	MTL (μm) ± se	MTL Std dev.	Dpar (μm)
Eastern MHA	**NS0402**	1,029	0.45	0.47	0.81	141 ± 2	100	7	13 ± 0.2	0.7	1.7 ± 0.2
Northern	*Metapelite*		*543*	*562*	*(N/A)*	*20*			*173*		
Foreland	**NS0404**	1,278	1.02	0.94	0.8	153 ± 9	73	13	12.1 ± 0.3	0.9	1.6 ± 0.2
	Sandstone		*682*	*626*	*(N/A)*	*25*			*229*		
North Atlas Front			***North Atlas Front***								
Inner Belt	**08OU***	1,100	0.14	0.70	0.40	13 ± 1	100	22	13.2 ± 0.4	2.2	-
	Volcanodet		*121*	*613*	*15,672*	*14*			*31*		
	05OU	1,230	0.19	1.27	0.40	9 ± 1	62	39	-	-	-
	Gneiss		*408*	*2,747*	*15,672*	*19*			-		
	OU0507*	1,338	0.38	5.55	0.76	9 ± 1	83	75	14.1 ± 0.2	0.8	2.3 ± 0.3
	Eyed-Gneiss		*549*	*8,097*	*(N/A)*	*20*			*195*		
	13OU	1,265	0.33	1.49	0.40	14 ± 1	65	46	-	-	-
	Gneiss		*486*	*2,180*	*15,672*	*17*			-		
	01OU	1,360	0.35	1.57	0.40	14 ± 1	66	48	-	-	-
	Gneiss		*519*	*2298*	*15,672*	*17*			-		
	TO0401	1,941	0.92	1.34	0.77	98 ± 9	52	22	11.3 ± 0.3	2.1	1.6 ± 0.4
	Granite		*1,043*	*1,525*	*(N/A)*	*22*			*120*		
	TO0402	2,291	0.94	0.98	0.76	132 ± 3	100	18	13 ± 0.2	1.7	1.7 ± 0.1
	Granite		*1,165*	*1,214*	*(N/A)*	*18*			*249*		
	17OU	1,480	0.35	1.91	0.40	12 ± 1	75	59	-	-	-
	Granodio		*436*	*2,356*	*15,672*	*14*			-		
	OU0506*	1,795	0.25	1.64	0.82	22 ± 1	99	24	13.7 ± 0.2	1.0	2.2 ± 0.3
	Eyed-Gneiss		*252*	*1,687*	*(N/A)*	*20*			*245*		
	15OU	1,580	0.25	1.21	0.40	13 ± 1	95	37	-	-	-
	Granodiorite		*261*	*1,253*	*15,672*	*15*			-		
	14OU*	1,560	0.9	3.35	0.40	17 ± 1	80	104	13.2 ± 0.3	2.3	-
	Eyed-Gneiss		*715*	*2,675*	*15672*	*18*			*48*		
	20OU*	1,520	0.63	2.83	0.41	15 ± 1	82	84	13.9 ± 0.2	1.6	-
	Amphibolt		*450*	*2,027*	*15,672*	*10*			*60*		
	TO0403*	2,544	0.08	0.90	0.75	13 ± 1	100	20	12.9 ± 0.2	1.4	1.6 ± 0.2
	Rhyolite		*81*	*909*	*(N/A)*	*20*			*166*		
	TO0404*	2,937	0.24	1.19	0.82	30 ± 3	79	56	12.5 ± 0.2	2.1	1.7 ± 0.1
	Rhyolite		*1,457*	*7,148*	*(N/A)*	*56*			*199*		
	OU0505*	2,549	0.28	2.35	0.79	17 ± 3	95	31	13.7 ± 0.1	0.8	2.2 ± 0.2
	Granite		*719*	*6,074*	*(N/A)*	*22*			*152*		
	OU0504*	2,722	0.40	2.79	0.78	20 ± 4	100	37	14 ± 0.1	0.8	2.1 ± 0.4
	Granite		*422*	*2,969*	*(N/A)*	*21*			*172*		
	OU0503*	2,883	0.43	2.11	0.79	30 ± 1	100	28	13.4 ± 0.2	0.6	1.9 ± 0.3
	Granite		*1,057*	*5,184*	*(N/A)*	*26*			*226*		
	OU0502*	3,000	0.46	2.00	0.78	33 ± 1	95	26	13.6 ± 0.1	1.0	2.3 ± 0.3
	Granite		*939*	*4,117*	*(N/A)*	*20*			*238*		
	TO0405*	2,500	0.06	0.19	0.83	44 ± 2	100	16	12.7 ± 0.2	2.0	2 ± 0.3
	Granite		*94*	*312*	*(N/A)*	*16*			*182*		
	2SA	2,150	0.19	0.37	0.43	27 ± 3	75	8	-	-	-
	Volcanodet		*174*	*329*	*2,127*	*18*			-		
	1SA	1,900	0.14	0.29	0.43	25 ± 3	100	17	-	-	-

AGU Tectonics

10.1002/2017TC004693

Table 1. *(continued)*

	Sample *Rock type*	Elevation (m)	ρ_s (10^6 tr/cm^2)	ρ_i (10^6 tr/cm^2)	ρ_d (10^6 tr/cm^2)	Central age (ma) ± 1σ	$P(\chi^2)$ %	U (ppm)	MTL (μm) ± se	MTL Std dev.	Dpar (μm)
	Volcanodet.		*79*	*163*	*2,127*	*17*					
South Atlas Front			***South Atlas Front***								
Southern	**01Si**	2,100	0.85	0.47	0.22	48 ± 3	38	*(N/A)*	-	-	-
Foreland	*Volcanodet.*		*1,005*	*563*	*16,656*	*22*					
Block SF1	**TO0407**	1,686	0.64	1.21	0.77	73 ± 1	100	20	12.5 ± 0.2	2.4	1.8 ± 0.1
	Granite		*1,125*	*2,148*	*(N/A)*	*20*			258		
	T00409	1,333	0.65	1.24	0.77	73 ± 1	100	17	12.6 ± 0.3	2.6	1.7 ± 0.1
	Granite		*1,112*	*2,134*	*(N/A)*	*20*			257		
	2Si	1,340	0.97	0.56	0.43	88 ± 5	60	*(N/A)*	-	-	-
	Granite		*973*	*563*	*2,127*	*19*					
	T00410	1,088	1.17	1.25	0.79	134 ± 3	100	17	13.2 ± 0.2	2.5	1.8 ± 0.2
	Granite		*1,416*	*1,513*	*(N/A)*	*35*			175		
Southern	**4Si**	2,150	0.20	0.39	0.43	27 ± 2	79	*(N/A)*	-	-	-
Foreland	*Granite*		*242*	*464*	*2,127*	*55*			-		
Block SF2	**3Si**	2,130	1.40	1.13	0.43	63 ± 4	46	*(N/A)*	-	-	-
	Granite		*848*	*686*	*2127*	*20*			-		
	SI0401	1,931	1.46	2.07	0.74	97 ± 5	92	22	12.6 ± 0.3	2.9	1.7 ± 0.2
	Granite		*413*	*585*	*(N/A)*	*20*			242		
Southern	**SI0402**	1,965	0.48	0.55	0.78	128 ± 5	88	9	13.1 ± 0.3	1.1	1.8 ± 0.2
Foreland	*Granite*		*356*	*404*	*(N/A)*	*21*			141		
Block SF3	**SI0404**	1,355	0.61	0.60	0.82	147 ± 2	100	8	13.5 ± 0.2	0.9	1.8 ± 0.3
	Matr. Congl.		*1,205*	*1,182*	*(N/A)*	*20*			231		
	SI0405	1,355	5.01	4.96	0.80	145 ± 2	99	65	13.2 ± 0.2	0.9	1.7 ± 0.2
	Pebble Congl.		*5,189*	*5,138*	*(N/A)*	*20*			235		
Western MHA	**BO01**	860	0.948	0.638	0.655	177 ± 13	44	12	11.3 ± 0.2	1.2	1.5 ± 0.2
	Granite		*565*	*380*	*3,202*	*20*			*63*		
Block WB1	**AZ03**	1,820	0.699	0.635	0.651	131 ± 8	98	12	11.7 ± 0.2	1.4	1.7 ± 0.1
	Granite		*700*	*636*	*3,202*	*20*			*47*		
	AZ02	1,480	0.561	0.487	0.649	136 ± 9	83	9	11.2 ± 0.2	1.7	1.7 ± 0.1
	Granite		*575*	*499*	*3,202*	*20*			*17*		
	ALM01	2,065	0.464	1.596	0.647	35 ± 3	49	30	-	-	1.8 ± 0.2
Block WB2	*Diorite*		*233*	*801*	*3,202*	*20*			-		
	AD01	1,135	0.842	7.242	0.653	14 ± 1	7	135	12.6 ± 0.2	1.7	1.7 ± 0.1
	Granite		*303*	*2,607*	*3,202*	*20*			*90*		

Note. ρ, density of tracks (*s* and *i* indicate spontaneous and induced densities, respectively, in apatite crystals and the mica detector, and *d* indicates the track density of the neutron glass monitor (CN5)). Densities are expressed in 10^5 t cm^{-2}. *Ns*, *Ni*, and *Nd* are the number of counted tracks for ρs, ρi, and ρd, respectively, given in italics below the density values. MTL, mean track length. Values in italics below the central age and MTL are, respectively, the number of single-grain ages and the number of lengths measured. 1σ is the standard deviation. Dpar corresponds to a kinetic factor determined for each sample (Barbarand et al., 2003). Samples used for the inner belt thermal modeling are labeled with "*." Shaded in gray are presented the elevation-corrected samples for the thermal modeling.

Table 2
AHe Results

	Name	Elevation (m)	*Rs* (μm)	Weight (μg)	*FT*	4He (ncc/g)	U (ppm)	Th (ppm)	Th/U	eU (ppm)	Age (ma)	Age c. (ma)
Eastern MHA												
Northern Foreland	**NS0401A**	1029	64	6	0.74	47,694.5	4.2	15.7	3.7	8	49	87 ± 5
	NS0401B		47	2.3	0.67	848,321.9	110.9	104.4	0.9	136	52	78 ± 3
	NS0401C		42	1.8	0.59	36,799.3	5.7	16.7	3	9.7	31	52 ± 4
	NS0401D		44	1.8	0.59	34,742.5	4.8	11.2	2.3	7.5	38	64 ± 4
	NS0402A	1029	39	2.3	0.59	258,846.9	21.8	17	0.8	25.9	81	136 ± 5
	NS0402B		35	1.0	0.53	152,129.7	9.9	43.6	4.4	20.4	62	116 ± 10
	NS0402C		39.5	1.8	0.60	294,060.8	23.7	22.3	0.9	29	81	135 ± 6
	NS0402D		35	1.3	0.58	68,886.4	5.1	17.6	3.5	9.3	60	102 ± 7
	NS0403A	1067	57.5	3.9	0.72	25,656.0	1.7	1.3	0.7	2	102	141 ± 9
	NS0403B		42	2.5	0.62	84,449.4	11.6	26.2	2.3	17.9	42	67 ± 5
	NS0403C		48.5	2.4	0.68	122,571.6	25	9.2	0.4	27.2	36	54 ± 2
	NS0404A	1278	54	3.4	0.70	115,655.8	36.6	39.5	1.1	46.1	21	30 ± 1
	NS0404B		54	4.4	0.69	27,288.7	13.9	37	2.7	22.8	10	14 ± 1
	NS0404C		77	9.6	0.78	37,417.7	7.7	16.8	2.2	11.7	26	34 ± 2
	NS0404D		69.5	7.5	0.75	10,566.2	4.4	16.8	3.8	8.4	10	14 ± 1
	NS0404E		52	3.2	0.69	126,011.2	31.1	37.2	1.2	40	26	38 ± 2
	NS0404F		69.5	7.5	0.76	38,022.2	18.6	16.5	0.9	22.6	14	18 ± 1
	NS0404G		69.5	7.5	0.76	38,022.2	21.6	19.2	0.9	26.2	12	16 ± 1
Inner Belt												
*OU0507**	**OU0507A**	1338	125	41.4	0.87	72,022.8	46.5	7.8	0.2	48.4	12	14 ± 2
	OU0507B		131	47.8	0.87	40,818.8	28.9	5	0.2	30.1	11	13 ± 2
	OU0507C		129.5	46.0	0.87	54,597.1	45.7	16.5	0.4	50	9	10 ± 1
	OU0507D		127	45.9	0.87	38,584.6	41.9	7.6	0.2	43.7	7	8 ± 1
TO0401	**TO0401A**	1941	59	5.6	0.72	11,167.2	9.7	16.5	1.7	13.7	7	10 ± 1
	TO0401B		62	5.8	0.74	15,819.6	16.3	14.7	0.9	19.8	7	9 ± 0
	TO0401C		58	4.4	0.72	23,195.4	21.2	15.4	0.7	25	8	11 ± 0
	TO0401D		65	6.4	0.75	18,761.0	17.6	14.1	0.8	21	7	10 ± 0
	TO0401E		47.5	2.6	0.67	29,247.9	32.5	18.7	0.6	37	7	10 ± 0
	TO0401F		57	5.1	0.71	38,257.7	37	31.3	0.8	44.5	7	10 ± 0
TO0402	**TO0402A**	2291	27	0.5	0.46	67,490.4	8.3	5.4	0.7	9.6	58	125 ± 10
	TO0402B		39	1.5	0.60	112,065.5	10.6	10.6	1	13.1	68	113 ± 6
	TO0402C		38	1.1	0.60	31,927.8	3.4	1.7	0.5	3.8	68	113 ± 4
*OU0506**	**OU0506A**	1795	86	14.1	0.80	21,218.1	2.7	2.9	1.1	3.4	51	64 ± 7
	OU0506B		77	9.8	0.78	7,297.4	5.1	8.5	1.7	7.1	9	11 ± 1
	OU0506C		66	6.8	0.75	10,123.7	8.2	13.3	1.6	11.4	7	10 ± 1
TO0403*	**TO0403A**	2544	71.5	7.6	0.77	8,649.8	4.2	6.2	1.5	5.7	13	17 ± 1
	TO0403B		93	17.0	0.82	9,770.4	4.4	6.3	1.4	5.9	13	16 ± 1
	TO0403C		71	7.3	0.77	7,730.5	3.5	5.7	1.6	4.9	13	17 ± 1
	TO0403D		100	20.0	0.83	7,704.5	3.4	5.1	1.5	4.6	14	17 ± 1
	TO0403E		41	1.7	0.62	24,190.6	15.8	19	1.2	20.4	10	16 ± 1
	TO0403F		36	1.1	0.58	54,395.4	45.7	20.9	0.5	50.7	9	15 ± 1
TO0404*	**TO0404A**	2937	37	1.3	0.58	19,780.8	9	9.7	1.1	11.3	15	26 ± 2
	TO0404B		35	1.0	0.56	52,630.8	22.9	47.4	2.1	34.3	12	22 ± 1
	TO0404C		47	2.5	0.66	41,624.3	14.7	28.8	2	21.6	16	24 ± 2
	TO0404D		82	13.0	0.79	2,516.9	0.8	1.6	2	1.2	17	22 ± 1
OU0505*	**OU0505A**	2549	105	25.2	0.84	37,799.9	16.2	21.2	1.3	21.2	15	18 ± 2
	OU0505B		81	11.5	0.79	30,278.6	12.7	18.9	1.5	17.2	15	18 ± 2
	OU0505C		104	24.0	0.84	31,893.6	14.7	18	1.2	19	14	16 ± 2
OU0504*	**OU0504A**	2722	70	8.2	0.76	22,127.1	12.5	31.5	2.5	20	9	12 ± 2
	OU0504B		73.5	8.2	0.78	56,687.6	27	33.7	1.2	35.1	13	17 ± 2
	OU0504C		87	13.6	0.81	37,742.6	17.8	20.3	1.1	22.7	14	17 ± 2
OU0503*	**OU0503A**	2883	116.5	32.4	0.86	39,838.1	15.7	17.3	1.1	19.9	17	19 ± 2
	OU0503B		119.5	34.6	0.86	43,956.3	15.8	20	1.3	20.6	18	21 ± 2
	OU0503C		115	31.4	0.85	35,052.3	12.4	15.1	1.2	16	18	21 ± 3
OU0502*	**OU0502A**	3000	101	22.0	0.83	54,122.5	20.5	22.7	1.1	25.9	17	21 ± 2

Table 2. *(continued)*

	Name	Elevation (m)	*Rs* (μm)	Weight (μg)	*FT*	4He (ncc/g)	U (ppm)	Th (ppm)	Th/U	eU (ppm)	Age (ma)	Age c. (ma)
	OU0502B		91	1.7	0.81	582,104.9	23.8	27.1	1.1	30.3	16	20 ± 2
	OU0502C		77	9.9	0.79	58,206.6	24.7	24.6	1	30.6	16	20 ± 2
OU0501*	**OU0501A**	3150	50	3.2	0.68	50,341.9	22.9	23.1	1	28.4	15	22 ± 3
*TO0405**	**TO0405A**	2500	40	1.5	0.60	15,275.6	8.5	10.2	1.2	10.9	11	19 ± 1
	TO0405B		31.5	0.8	0.52	26,478.9	18.2	16.9	0.9	22.3	10	19 ± 2
	TO0405C		36.5	1.3	0.58	16,779.0	9	6.7	0.7	10.6	13	22 ± 1
*TO0406**	**TO0406A**	1934	36	1.3	0.57	15,624.5	9.7	12.1	1.3	12.6	10	18 ± 1
	TO0406B		36	1.2	0.55	21,596.0	12.6	43.8	3.5	23.1	8	14 ± 1
	TO0406C		37	1.4	0.56	24,871.7	15.2	46.5	3.1	26.4	8	14 ± 2
	TO0406D		34.5	1.2	0.55	15,092.2	10.5	6	0.6	11.9	10	18 ± 1
	TO0406E		36	1.2	0.55	21,596.0	12.6	43.8	3.5	23.1	8	14 ± 1
*OK1**	**OK1A**	2794	56.1	4.9	0.75	6,880	5.8	7.4	1.3	7.6	8	10 ± 1
	OK1B		55.5	4.0	0.75	3,396.9	1.8	11.1	6.1	4.5	6	8 ± 1
*OK2**	**OK2A**	2460	65	6.7	0.78	23,472	29.7	38.6	1.3	39	5	6 ± 1
	OK2B		57.1	4.2	0.76	58,128.6	38.3	57.3	1.5	52	9	12 ± 1
	OK2C		47.7	2.8	0.71	47,335.6	58.9	72.7	1.2	76.3	5	7 ± 1
	OK2D		45.8	2.4	0.70	50,561.5	37.2	63.4	1.7	52.4	8	11 ± 1
Southern Foreland Unit SF1												
TO0408	**TO0408A**	1555	53	4.0	0.69	38,022.2	28	28.1	1	34.7	9	13 ± 1
	TO0408B		53.5	3.6	0.70	38,911.6	28.5	23.6	0.8	34.2	10	14 ± 1
	TO0408C		52.5	3.3	0.69	28,046.7	21.8	19.5	0.9	26.5	9	13 ± 1
	TO0408D		56.5	3.9	0.71	22,295.1	13.7	11.9	0.9	16.6	11	15 ± 1
TO0407	**TO0407A**	1686	50	3.8	0.68	28,437.7	23.7	18.8	0.8	28.2	8	12 ± 1
	TO0407B		51.5	3.3	0.69	40,629.8	36.1	31.6	0.9	43.7	8	11 ± 1
	TO0407C		95.5	18.0	0.82	26,348.7	15.8	17.2	1.1	19.9	11	13 ± 1
TO0409	**TO0409A**	1333	45.5	2.2	0.65	63,218.8	21.5	22.9	1.1	27	19	29 ± 1
	TO0409B		40	1.9	0.61	19,011.1	8	7.4	0.9	9.8	16	27 ± 1
	TO0409C		26	0.5	0.45	113,462.5	59	36.5	0.6	67.8	14	31 ± 2
	TO0409D		49.5	2.5	0.68	18,210.6	6.2	4.9	0.8	7.4	20	30 ± 1
TO0410	**TO0410A**	1088	39	1.4	0.61	50,029.2	11.4	3	0.3	12.1	35	57 ± 2
	TO0410B		35	1.1	0.55	254,694.3	36.8	57.8	1.6	50.7	43	78 ± 5
	TO0410C		43	1.8	0.64	83,937.9	15.6	7.2	0.6	17.3	41	63 ± 2
	TO0410D		29	0.7	0.48	48,314.00	8.1	9.5	1.2	10.4	39	80 ± 6
	TO0410E		43	1.7	0.64	127,133.1	19.8	2.8	0.1	20.5	51	79 ± 2
	TO0410F		39	1.4	0.59	110,064.3	13	27.3	2.1	19.6	48	79 ± 5
	TO0410G		60	4.5	0.73	56,255.1	6	8.3	1.4	8	58	79 ± 4
Southern Foreland Unit SF2												
Ask7	**Ask7A**	2280	41.1	1.7	0.67	184,174	60	75.4	1.3	78	20	29 ± 2
	Ask7B		45.8	2.4	0.70	314,605.6	103.1	76.4	0.7	121.5	21	29 ± 2
	Ask7D		45	2.2	0.69	370,706.6	140.4	110.4	0.8	166.9	18	25 ± 2
	Ask7E		45	2.2	0.69	152,891.4	73.1	49.4	0.7	84.9	15	21 ± 2
Ask6	**Ask6A**	2380	55.3	3.8	0.75	712,335.2	159	64	0.4	174.3	34	46 ± 4
	Ask6B		46	2.4	0.70	644,109.2	86.9	56.9	0.7	100.5	53	78 ± 6
	Ask6C		31.2	0.8	0.57	746,792.8	72.6	148.5	2	108.3	57	103 ± 8
	Ask6D		41.5	1.9	0.67	309,507	65.9	88.9	1.3	87.2	29	45 ± 4
	Ask6E		39	1.6	0.65	1,230,733.6	441.4	136.9	0.3	474.2	21	34 ± 3
Ask5	**Ask5A**	2100	55.2	4.6	0.74	211,460.3	88.2	71.4	0.8	105.3	17	23 ± 2
	Ask5B		43.5	2.0	0.69	210,889.1	149.3	101.9	0.7	173.8	10	14 ± 1
	Ask5C		40.1	1.6	0.66	646,995.8	127.1	133.2	1	159.1	34	53 ± 4
	Ask5D		44.6	2.1	0.69	245,705.4	53.1	52.8	1	65.8	31	43 ± 3
	Ask5E		43.4	2.4	0.68	108,266.4	143.9	56.1	0.4	157.4	6	8 ± 1
Ask4	**Ask4A**	1910	48.8	2.6	0.72	209,821.1	45.8	56.7	1.2	59.4	29	39 ± 3
	Ask4B		61.5	5.3	0.77	179,607.8	55.1	39.1	0.7	64.5	23	30 ± 2
	Ask4C		47.4	2.6	0.71	597,680.9	88.2	731.4	8.3	263.8	19	28 ± 2
	Ask4D		55.6	4.0	0.75	451,292.8	100.6	79.2	0.8	119.6	31	44 ± 4
	Ask4E		49.5	2.9	0.72	306,556.7	63.1	69.9	1.1	79.9	32	46 ± 4

Table 2. *(continued)*

	Name	Elevation (m)	*Rs* (μm)	Weight (μg)	*FT*	4He (ncc/g)	U (ppm)	Th (ppm)	Th/U	eU (ppm)	Age (ma)	Age c. (ma)
Ask3	**Ask3A**	1920	45	2.2	0.69	70,547	29.2	37.3	1.3	38.1	15	20 ± 2
	Ask3B		40.7	1.8	0.66	70,743.5	18.3	31.6	1.7	25.9	23	33 ± 3
	Ask3D		53.5	4.2	0.74	113,348.9	31	50	1.6	43	22	29 ± 2
	Ask3E		47.9	2.6	0.71	93,940.2	18	34	1.9	26.1	30	41 ± 3
SI0401	**SI0401A**	1931	69	7.5	0.76	102,993.5	24.6	25.8	1	30.8	28	36 ± 2
	SI0401B		69	7.2	0.61	31,824.2	7.4	8.2	1.1	9.4	28	46 ± 2
	SI0401C		45	2.1	0.64	67,658.6	5.6	18.3	3.3	10	57	90 ± 7
	SI0401D		45	2.1	0.64	7.67E + 10	8.8	20.8	2.4	13.8	58	91 ± 6
	SI0401E		37.5	1.3	0.59	127,767	41.4	40.6	1	51.1	21	36 ± 2
	SI0401F		36	1.2	0.58	137,580.4	39.5	26.8	0.7	45.9	25	43 ± 2
	SI0401G		43	1.7	0.63	19,599.7	2.6	1.1	0.4	2.9	56	88 ± 3
Southern Foreland Unit SF3												
SI0402	**SI0402A**	1965	57.5	4.3	0.71	47,702.3	7.3	12.7	1.8	10.3	38	53 ± 3
	SI0402B		46	2.7	0.64	53,735.1	8	19	2.4	12.6	35	55 ± 4
	SI0402C		45.5	2.2	0.65	68,221.7	11.8	19.6	1.7	16.5	34	52 ± 3
	SI0402D		50	2.8	0.67	105,418.8	17.1	37.3	2.2	26.1	34	50 ± 3
	SI0402E		51	3.2	0.68	52,530.7	7.6	18	2.4	11.9	37	54 ± 4
	SI0402F		78	10.0	0.79	19,811.6	2.8	3.5	1.2	3.6	44	56 ± 3
Ask2	**Ask2A**	1930	48.8	2.6	0.72	44,322.5	4	16.6	4.1	8	46	57 ± 5
	Ask2B		41.8	1.7	0.67	39,733.8	1.9	22	11.5	7.2	46	62 ± 5
	Ask2D		42.4	1.7	0.68	43,545.3	3.3	18.5	5.6	7.8	47	62 ± 5
	Ask2E		38.9	1.4	0.65	17,508.7	4.5	25.4	5.6	10.6	14	21 ± 2
SI0403	**SI0403A**	1822	43	1.6	0.63	46,026.9	13.3	14.2	1.1	16.7	23	36 ± 2
	SI0403B		43.5	1.8	0.65	44,192.5	12.9	9.7	0.7	15.2	24	37 ± 3
SI0404	**SI0404A**	1355	41	2.0	0.62	438,756.4	84	3.7	0	84.9	42	55 ± 1
	SI0404B		43	1.9	0.63	53,715.6	5.1	9.1	1.8	7.3	60	96 ± 6
	SI0404C		36	1.1	0.57	79,046.2	14.1	26.9	1.9	20.6	32	56 ± 3
	SI0404D		37	1.2	0.57	224,297.8	40.4	81.8	2	60	32	56 ± 4
SI0405	**SI0405A**	1355	79.5	11	0.80	1,955,688.5	345.4	3.0	0	346.1	46	58 ± 1
	SI0405B		81	12	0.80	2,609,858.7	178.6	2.6	0	179.2	121	152 ± 3
	SI0405C		82.5	13	0.80	1,985,776	215.9	3.1	0	216.6	76	95 ± 2
	SI0405D		72.5	7.9	0.78	2,381,138.6	176	1.9	0	176.5	109	141 ± 3
	SI0405E		77	9.6	0.79	1,938,633.1	142.6	1.7	0	143	110	139 ± 4
Western MHA ***Unit WB1***												
BO01	**BO01A**	860	36.1	0.97	0.670	221,202.6	20.1	27.1	1.3	26.6	68	102 ± 8
	BO01B		32.2	0.83	0.662	17,054.6	3.4	16.6	4.9	7.3	19	29 ± 2
	BO01C		45.6	1.85	0.754	240,361.4	16.9	37.3	2.2	25.8	77	101 ± 8
	BO01D		38.9	1.34	0.737	29,614.0	2.6	10.7	4.1	5.2	47	64 ± 5
AZ03	**AZ03A**	1820	42.5	1.95	0.701	288,493.1	12.3	76.3	6.2	30.6	78	111 ± 9
	AZ03B		43.1	1.80	0.712	152,635.0	7.5	55.6	7.4	20.9	60	85 ± 7
	AZ03D		59.0	4.42	0.791	370,907.3	14.5	101.0	7.0	38.7	79	100 ± 8
	AZ03E		55.0	3.55	0.776	643,837.4	14.6	78.1	5.4	33.3	159	205 ± 16
	AZ03F		63.7	5.17	0.811	355,472.8	12.8	76.5	6.0	31.1	94	116 ± 9
	AZ03G		39.4	1.31	0.691	137,862.0	12.8	83.6	6.5	32.8	35	50 ± 4
	AZ03H		65.2	7.66	0.800	512,651.3	10.7	75.4	7.0	28.8	147	184 ± 15
	AZ03I		57.9	4.06	0.788	290,080.6	11.0	69.5	6.3	27.7	87	110 ± 9
	AZ03L		73.2	7.83	0.835	548,649.1	17.6	107.4	6.1	43.4	104	125 ± 10
AZ04	**AZ04B**	1750	80.8	11.85	0.873	294,008.0	26.8	54.0	2.0	39.7	61	70 ± 6
	AZ04C		53.6	3.43	0.767	637,710.9	16.2	80.2	4.9	35.4	148	193 ± 15
	AZ04E		89.1	16.00	0.886	527,447.4	13.7	63.1	4.6	28.8	151	170 ± 14
AZ01	**AZ01A**	1480	37.8	1.14	0.689	254,295.5	16.5	87.7	5.3	37.5	56	81 ± 6
	AZ01B		65.0	5.71	0.812	311,565.1	14.5	58.7	4,0	28.6	90	110 ± 9
	AZ01C		43.1	1.60	0.726	1.764055.3	56.3	349.4	6.2	140.2	104	143 ± 11
	AZ01D		42.7	2.08	0.682	160,743.2	9.1	75.4	8.3	27.2	49	72 ± 6
	AZ01E		36.6	1.12	0.638	231,671.5	18.0	96.3	5.4	41.1	46	73 ± 6
	AZ01G		71.5	7.19	0.833	372,380.9	20.1	40.5	2.0	29.8	103	123 ± 10

Table 2. *(continued)*

	Name	Elevation (m)	*Rs* (μm)	Weight (μg)	*FT*	4He (ncc/g)	U (ppm)	Th (ppm)	Th/U	eU (ppm)	Age (ma)	Age c. (ma)
AZ02	**AZ02A**	1480	75.9	8.51	0.846	116,340.1	6.9	32.7	4.8	14.7	65	77 ± 6
	AZ02B		46.4	1.94	0.754	23,407.9	6.4	32.3	5.1	14.1	14	18 ± 1
	AZ02C		64.8	5.76	0.810	111,848.4	12.9	62.0	4.8	27.8	33	41 ± 3
	AZ02D		41	1.41	0.709	67,710.3	8.2	44.1	5.3	18.8	30	42 ± 3
	AZ02AA		29.7	0.54	0.607	178,448.0	14.1	68.4	4.9	30.5	48	79 ± 6
	AZ02BB		39.5	1.47	0.684	112,248.6	6.6	28.8	4.4	13.5	69	100 ± 8
	AZ02CC		34.3	0.9	0.647	127,869.8	8.1	35.0	4.3	16.5	64	98 ± 8
Unit WB2												
ALM01	**ALM01AA**	1950	71.7	10.86	0.815	37,056.6	19.6	9.4	0.5	21.8	14	17 ± 1
	ALM01BB		110.4	29.77	0.884	26,013.0	9.4	8.3	0.9	11.4	19	21 ± 2
	ALM01A		32.4	0.67	0.662	48,049.3	29.1	40.7	1.4	38.9	10	15 ± 1
	ALM01C		37.6	0.56	0.635	62,454.1	29.3	34.6	1.2	37.6	14	21 ± 2
	ALM01D		33.4	0.37	0.594	153,303.7	47.2	49.3	1.0	59.0	21	36 ± 3
	ALM01E		32.6	0.95	0.585	117,968.0	45.4	39.6	0.9	54.9	18	30 ± 2
ALM02	**ALM02A**	1950	36.7	0.99	0.682	23,926.0	24.2	20.2	0.8	29.0	7	10 ± 1
	ALM02B		37.9	1.28	0.722	64,439.7	22.2	28.4	1.3	29.0	18	25 ± 2
	ALM02C		46.3	2.15	0.735	44,906.7	31.9	18.6	0.6	36.4	10	14 ± 1
	ALM02D		56.6	3.81	0.783	121,401.5	38.8	50.6	1.3	50.9	20	25 ± 2
AD01	**AD01A**	1135	117.1	20.85	0.877	150,457.5	201.7	8.4	0	203.7	6	7 ± 1
	AD01C		97.4	13.47	0.854	200,744.9	376.2	10.4	0	378.7	4	5
	AD01D		83.5	13.34	0.829	260,865.8	414.3	6.8	0	415.9	5	6
	AD01E		132.1	40.13	0.891	528,967.6	423.2	7.6	0	425.0	10	11 ± 1
	AD01F		110.4	33.78	0.872	959,257.5	538.3	9.5	0	540.6	14	17 ± 1
	AD01G		107.8	17.68	0.867	13,808.5	27.6	1.8	0.1	28.1	4	5
	AD01H		81.6	7.57	0.826	135,088.3	186.3	7.3	0	188.1	6	7 ± 1

Note. Rs (sphere equivalent radius) and FT (ejection factor) have been calculated using the procedure developed by Gautheron and Tassan-Got (2010) and Ketcham et al. (2011). eU (effective uranium) has been calculated with the formula [eU] = [U] + 0.24 × [Th] + 0.008 × [Sm]. "Age c." means (U-Th-Sm)/He age corrected for alpha ejection with the FT. The error is estimated to be a maximum of 8%. ncc, nano cubic centimer. Same legend as Table 1 for "*" label and the gray shades.

trend (Figure 6a). In comparison, the vertical distribution of MTLs does not show any significant variations within error bars (Figure 6b).

Single-grain AHe ages of 15 samples range from 6 ± 1 to 125 ± 10 Ma (Table 2). Four single-grain AHe ages of 53 are significantly older (from 67 ± 4 to 125 ± 10 Ma; TO0402 sample and one replicate of the OU0506 sample) and not used for modeling. All other single-grain AHe ages range from 6 ± 1 to 26 ± 2 Ma. As for the AFT ages, mean AHe ages display a clear relationship with elevation despite being younger, and coherently, we took into account the vertical offset of the same shifted samples as we did for the AFT data set (Figures 6c, 3b, and 3c).

4.1.3. Southern Foreland

Based on the single-grain AHe age reproduction among samples and the structural network, the southern foreland is divided into three units: a northern unit SF1, where single-grain AHe ages show good reproduction, and central SF2 and southern SF3 units, where single-grain AHe ages display a complex scattering (Figures 3b and 3c, Table 2, and Figure S2).

We use 11 AFT ages for the Askaoun-Siroua plateau (Ghorbal, 2009; Missenard et al., 2008) (Figure 2). AFT ages range from 27 ± 7 to 147 ± 2 Ma (Table 1). Close to the SAF, they range from 48 ± 3 to 88 ± 5 Ma (Figures 2, 3b, and 3c). They display minimum AFT ages 20–30 km from the SAF before getting "older" as samples get farther from the SAF. MTLs show an important scattering, from 9.8 ± 0.3 to 13.5 ± 0.2 μm, while the TLDs are spread and complex. Dpar ranges from 1.1 ± 0.3 to 1.9 ± 0.3 μm.

The 69 single-grain AHe ages range from 8 ± 1 to 152 ± 3 Ma (Table 2). Most AHe ages are equal or younger than 90 Ma (62 of 69 AHe ages) and always younger than AFT ages. Apart from the samples close to the SAF (TO0407 to TO0410), which show good reproduction of single-grain AHe ages, southernmost samples from units SF2 and SF3 display a complex scattering of single-grain AHe ages (Table 2 and Figure S2).

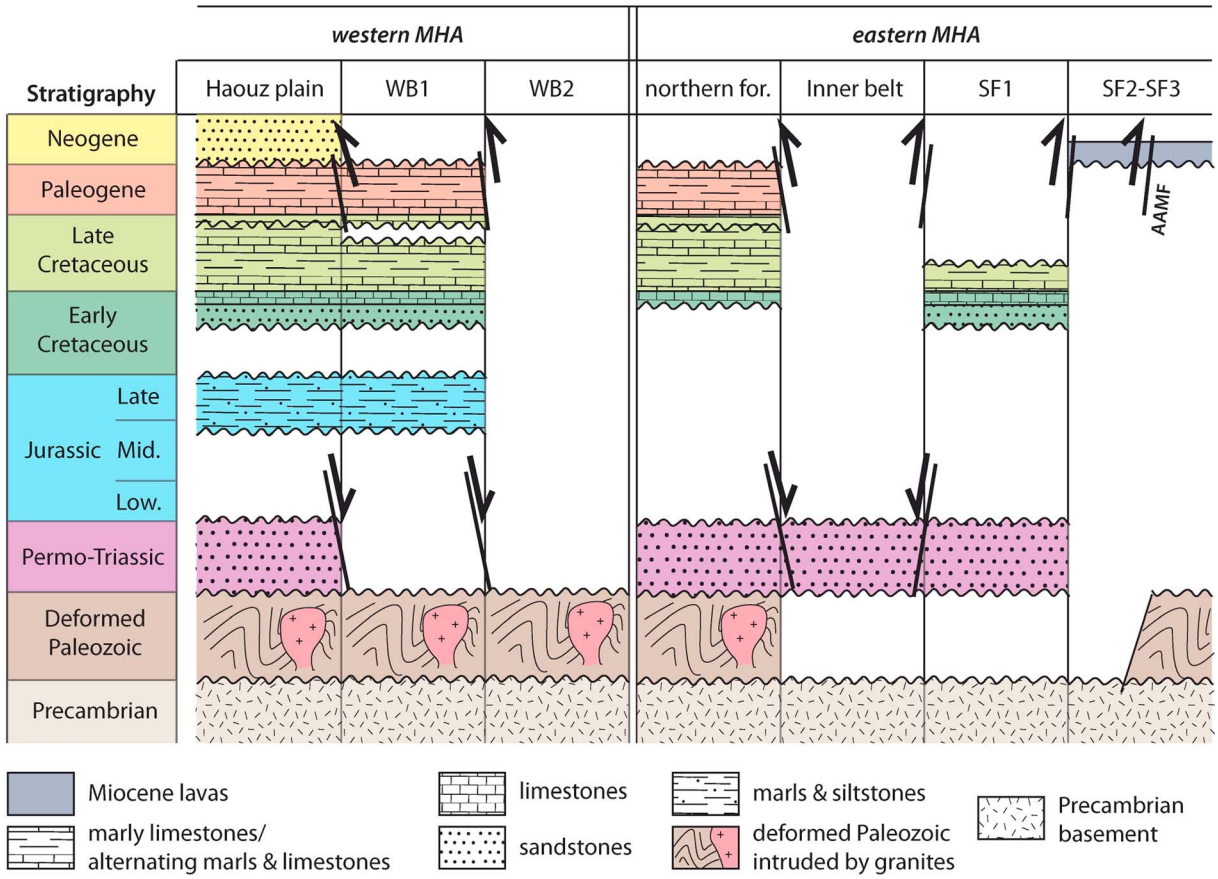

Figure 5. Tectono-stratigraphic chart giving the stratigraphical successions in each structural unit defined in the text and in Figure 3. It is based on the geological map of Morocco by Hollard and Choubert (1985) and more specifically on Sinan (2000) for the subsurface formations in the Haouz Basin.

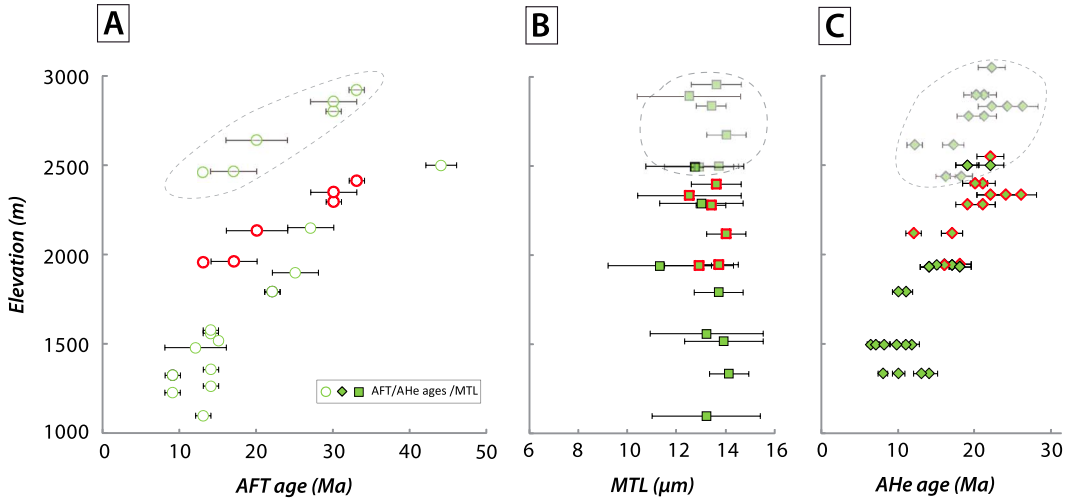

Figure 6. Data versus elevation plots for the inner belt, that is, the domain bounded by the SAF and the Sidi Fars Thrust (see Figure 2). (a, b) Age-elevation plots for AFT ages and MTL, respectively. (c) Age-elevation plot for AHe ages. In all plots, symbols with red contour show the samples corrected for elevation (see correspondence in Figure 2b and Tables 1 and 2). Their original position is represented in light grey.

4.2. Western MHA Transect

This cross section (Figures 3d and 3e) is segmented from north to south into WB1 and WB2 units (Figure 5).

AFT ages range from 14 ± 1 Ma to 177 ± 13 Ma (Figures 2a, 3d, and 3e and Table 1). MTLs range from 11.2 ± 0.2 to 12.6 ± 0.2 μm. The absence of long MTL values indicates complex thermal histories. TLDs are unimodal but broad (Figure S1). Dpar range from 1.4 ± 0.2 to 1.8 ± 0.2 μm.

Eight samples have mean AHe ages from 8 to 145 Ma, with a total dispersion ranging from 5 ± 1 to 206 ± 21 Ma. (Figures 2a, 3d, and 3e, Table 2, and Figure S3). The samples get younger toward the inner belt: AHe ages display a general negative relationship with the elevation with younger ages for the high-elevation samples of unit WB2 (Figures 2a, 3d, and 3e).

4.3. Thermal Modelings

4.3.1. Northern Foreland

We carried two inverse modeling in this area, using NS0401-02 samples in one hand and NS0404 on the other hand, the two groups of samples being separated by a fault (Figure 2a). Sample NS0303 was not modeled since its single-grain AHe ages display a negative AHe-eU relationship (Figure S2) attributed to the highly variable Th/U ratios (Table 2). Stratigraphical constraints were used for the modeling: (1) unconformable Triassic formations on the Paleozoic basement and (2) Lower Cretaceous formations unconformably overlying the Triassic formations (Figures 2a and 5).

Thermal modelings show low reproducibility of the data when both data sets (AFT and AHe) are considered (Figures S4 and S5). Thermal modeling of either the AFT or the AHe data set alone was done for each sample to check the sensibility of the modeling against modeling using both data sets (Figures S4 and S5). For inverse modeling with AFT data only, old AFT ages in both samples allow identifying a Triassic-Late Jurassic heating/cooling cycle, with reheating after the Early Cretaceous (Figures S4 and S5). On the contrary, inverse modelings with AHe data only are poorly sensitive to old events in function of the AHe ages range: for NS0401-02 the old AHe ages allow evidencing a Late Jurassic-Early Cretaceous cooling event not evidenced for NS0404 given its young AHe ages (Figure 7c, Table 2, and Figure S5).

The northern foreland records a cooling signal between Middle(?)-Late Jurassic and Early Cretaceous, followed by an early Late Cretaceous reheating whose amplitude is variably constrained, before a single Cenozoic cooling. Moreover, NS0404 sample, which is closer to the more internal Sidi Fars Thrust, may have undergone a stronger Cretaceous-Paleogene reset than NS0401-02 given its grouped single-grain AHe ages. This sample was also subjected to cooling only after 40 Ma.

4.3.2. Inner Belt of the Eastern MHA

Assuming that some samples are close to Triassic deposits (Figure 2a), we used (1) a large time-temperature box from 250 to 200 Ma with temperatures between 0 and 140°C and (2) from 200 to 100 Ma, temperature was assigned between 0 and 200°C, the 200°C value exceeding the closure temperatures of the AFT and AHe methods in order not to impose constraints during this period (Figure 8a).

Before 44 Ma, the modeling shows that the whole rock column had stayed at temperatures higher than 120°C. All LTT ages are younger than 44 Ma with long MTLs, which imposes the samples to be at temperatures higher than 110 ± 10°C before. From 44 Ma, three cooling steps are recognized. From 42–40 Ma to 35–33 Ma, a mean 100°C cooling is recorded by all samples (phase D1). A subsequent reheating of more than 30°C occurred until 18–20 Ma, before the second cooling phase D2. This cooling lasted from 23 to 18 Ma, with varied thermal amplitudes following the different elevations of the samples: the lowest and highest samples underwent a mean 93°C and 60°C cooling, respectively (Figure 8b). A weak 10–20°C reheating happened after 22–23 Ma up to the last D3 cooling phase, which, again, displays a high differentiation given the elevation of the samples: the highest and the lowest ones record a 30°C and a 110°C cooling, respectively (Figure 8b).

4.3.3. Southern Foreland

We used the following stratigraphical constraints (Figures 2 and 5): (1) unconformable Triassic formations on the Precambrian basement; (2) unconformable Cenomanian-Turonian formations on the basement, west of the Siroua Plateau; (3) Lower Cretaceous outcrops at the base of the Cenomanian-Turonian and the unconformity between Early Cretaceous and Triassic is known east of Eç Sour; and (4) the Miocene Siroua volcano lava unconformably covers the Precambrian basement.

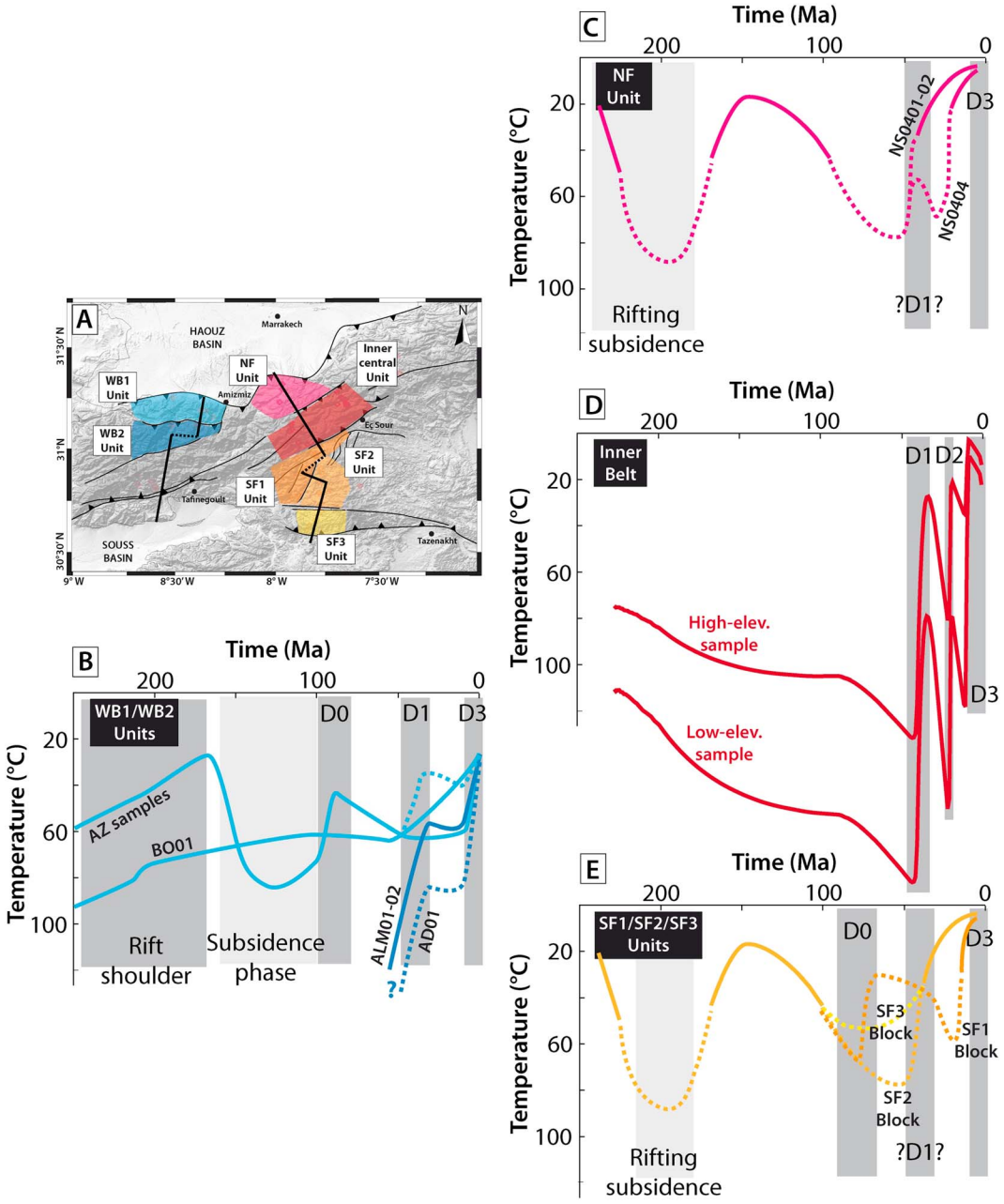

Figure 7. Results of the thermal modeling for the western and eastern MHA. (a) DEM of the area with location of cross sections and structural units. (b–e) Results of the inverse modeling for all structural domains: (b) for the WB2 unit in the western MHA, (c) for the northern foreland of the eastern MHA, (d) for the southern foreland of the eastern MHA, and (e) for the inner belt in the eastern MHA. The color code for thermal paths coincides with the colors for the samples in Figure 7a. Dark and light grey boxes behind the thermal paths correspond respectively to the cooling/erosion phases and to the (re)heating/subsiding phases.

As for the northern foreland (section 4.3.2), AFT and AHe data sets show a general discrepancy, preventing good modelings. Samples with either an AFT data set or an AHe one could be successfully modeled but are then not representative. Anomalously high eU content also prevented modeling (Ask5 to Ask7 samples; Table 2 and Figure S2) since they are not explained by the current models of Flowers et al. (2009) and Gautheron et al. (2009) (see Recanati et al., 2017). We interpret the results and describe them from SF1 to SF3 unit.

In SF1 unit, AFT age scattering is large, from 48 ± 3 to 134 ± 3 Ma and not explained through variations in lithology or elevation (Tables 1 and 2). Instead, single-grain AHe ages of some samples are well grouped

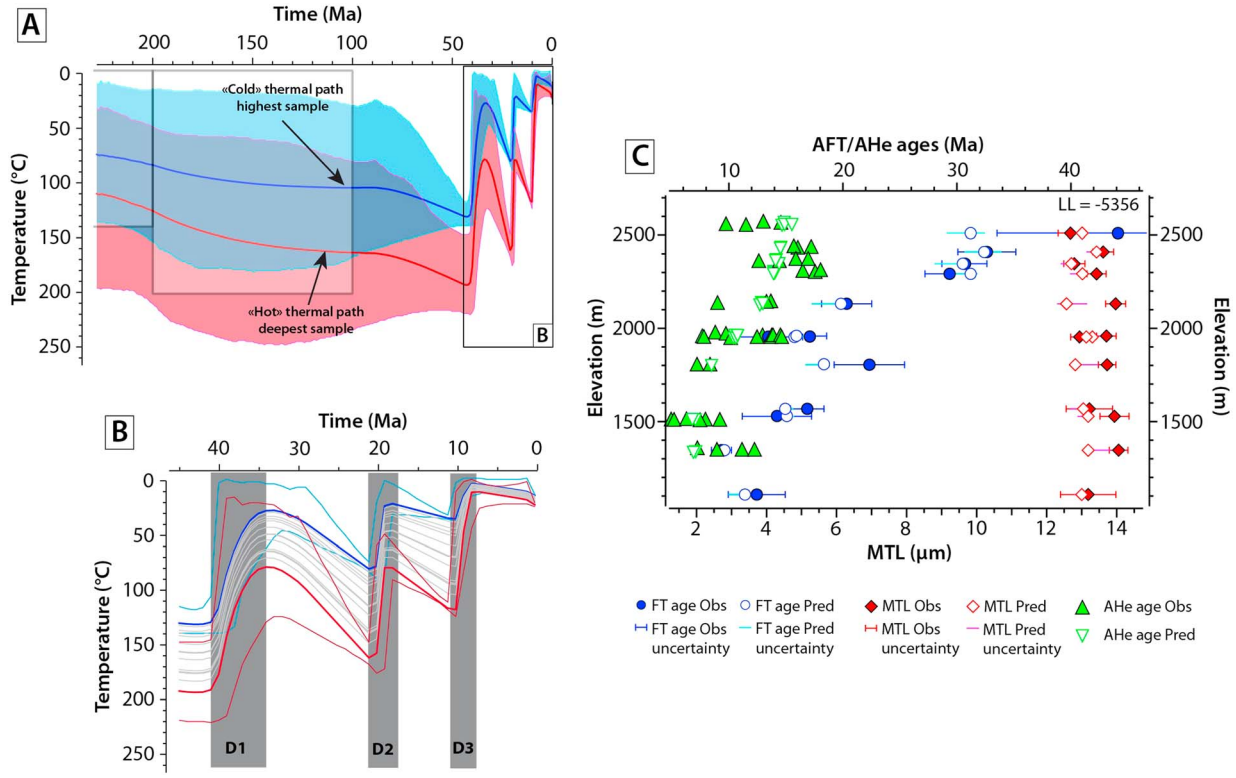

Figure 8. Results of the thermal modeling for the inner belt in the eastern MHA. (a) Best inverse thermal model for the pseudo-vertical section. Dark red and blue lines show the thermal histories for the deepest and the highest samples along the pseudovertical profile, respectively. Red and blue envelopes show the 95% credible intervals for the lowermost and uppermost samples, respectively. (b) Focus on the last 44 Ma of the thermal modeling presented in Figure 8a. Legend is the same except that we did not draw the envelopes and show the thermal paths of all the intermediate samples along the pseudovertical profile. (c) Summary predictions for the expect models.

(Table 2 and Figure S2). This roughly implies a quite rapid cooling through the PRZ at the considered age. The closest samples to the SAF (TO0408 and TO0407) show significant uplift from the end of the Miocene onward. For TO0409 and TO0410, uplifts occurred earlier in the Late Eocene–Oligocene and in the Late Cretaceous, respectively. Overall, samples very close to the SAF yielded the youngest AFT ages (TO0407-08 and 01-02Si) and might record a post-Cenomanian-Turonian uplift, although their AHe ages are younger mostly recording an early Miocene cooling event (Figure 7d). Farther from the SAF, TO0410 sample yielded AFT and AHe data sets difficult to reconcile with an early Late Cretaceous uplift given that its single-grain AHe ages are significantly younger, whatever the eU. It would imply a quick reheating after Early Cretaceous surface conditions up to the beginning of Late Cretaceous to partially reset the AFT age and almost completely the AHe ages (57–80 Ma).

On the SF2 and SF3 units, AFT ages get older southward, whereas the mean AHe ages within similar eU range are quite constant (Figures 3b, 3c, and S2). Single-grain AHe ages are grouped for the SF2 unit, whereas they seem to display an AHe age-eU positive relationship for the SF3 unit (Figure S2). Samples from the SF2 unit have been buried deeper after the Cenomanian-Turonian than the SF3 unit samples with stronger reset of the AFT thermochronometer and a complete reset for the AHe one (Figure 7d).

4.3.4. Western MHA

Different stratigraphical data were used for each structural unit. For the unit WB1 (Figures 2a, 3a, and 5) (1) an extended Middle Jurassic to Cenomanian-Turonian cover (~400 to 700 m thick) is preserved in sedimentary plateaus and (2) samples were at maximum depths of ~400–700 m since Eocene series are preserved on top.

We used two combined samples, AZ01-02 and AZ03-04, assuming similar elevations for each couple, and carried out a joint thermal modeling considering their difference in elevation within the same granite (detailed procedure in Text S2, Figure S6, and Table S2). After a slow cooling, samples reached surface temperatures by the end of the Jurassic (170 Ma; Figure 7b). It is followed by a 50°C heating phase

between 170 Ma and 140 Ma. A slow cooling occurred from 140 to 100–110 Ma, before a rapid 30°C cooling between 100 and 90 Ma. Renewed cooling intervened until Eocene times, and thermal quiescence is observed up to 10 Ma before a 30–35°C rapid cooling in the last 10 Ma. The sample BO01 displays a quite different thermal history maybe due to its peculiar position close the northern front (Figures 2a and 4, Text S3, and Figure S7): after stable thermal conditions during most of Mesozoic, it underwent cooling from 50 Ma onward (Figure 7b).

In WB2 unit, we modeled AD01 sample on one hand and the combined ALM01-02 sample (different elevations and same pluton) on the other hand. The inverse thermal modeling of ALM01-02 displays a 60–70°C cooling from 60 to ~30 Ma, followed by a slight reheating up to 12–10 Ma before the last 40°C cooling pulse (Figures 7b and S8). On the contrary, inverse thermal modeling for AD01 sample gave bad predictions. Assuming the present-day elevation difference (~900 m) and the associated temperature offset (~27°C with a commonly used value of 30°C.km^{-1} for the thermal gradient), forward models are found that fit data from WB2-3 and show that it has undergone a similar thermal history, with a temperature offset due to the elevation difference (Figures 4, 7b, and S9, Text S4, and Table S3).

5. Discussion

5.1. From Rift to Postrift Evolution of the MHA

In the studied area, there are no remnants of significant magmatic activity occurring during the Mesozoic-Cenozoic, with the exception of the Neogene Siroua volcanic activity (Figure 2a). The possibility of its influence has been discussed and discarded by Missenard et al. (2008). We also put forward that most of the samples from structural units SF2 and F3 do not show reset trends in their single-grain AHe ages (Figure S2), which is not in favor of a general reset. We thus consider that the cooling and heating trends recorded by the samples merely reflect erosion and burial.

The postrift evolution of the MHA began after the Early-Middle Jurassic. LTT ages being always younger than circa 150 Ma, that is, younger than formation age, evidence a significant burial of the samples before (sections 4.3.2 to 4.3.4). Also, other LTT and sedimentary studies advocated the existence of such a sedimentary infill of the Atlas rift in the Early-Middle Jurassic and at the scale of Northwest Morocco (Domènech et al., 2015, 2016; El Haimer, 2014; Ghorbal et al., 2008; Saddiqi et al., 2009)

5.1.1. The Middle(?)/Late Jurassic-Early Cretaceous Erosion Phase

The WB1 unit experienced a slow uplift since Middle Jurassic (Figure 7b), whereas no sedimentary remnants exist in the WB2 unit. The northern foreland of eastern MHA underwent a significant uplift in the Middle(?)/Late Jurassic-Early Cretaceous after a necessary subsiding phase during the rifting (previous section) which is in line with the Domènech et al. (2016) results using zircon LTT. In its southern foreland, with the exception of samples close to the SAF, most of the others underwent uplift during this period (Figures 7d and 9 and section 4.3.3).

This uplift is recognized on a much wider scale in different domains of Morocco (among others Saddiqi et al., 2009; Sehrt et al., 2018). Leprêtre, Missenard, Barbarand, et al. (2015) and Leprêtre et al. (2017) characterized this doming along the whole width of the Moroccan Atlantic passive margin (>500–600 km inland) and proposed mantle-related phenomenon linked to the Atlantic evolution.

5.1.2. From Early Cretaceous to Late Cretaceous

In the western MHA, the beginning of Early Cretaceous is marked by subsidence of WB1 unit (Figure 7b). For WB2 unit and the Tichka massif area (Figure 2a), we propose that samples also underwent the same subsidence, until the Late Cretaceous (Figure 9b).

At the beginning of the Late Cretaceous, an important erosion phase affected the northern flank of the belt (D0 phase in Figure 7). This erosion is not recorded in the WB2 unit, which was likely too deep to record it. We propose that samples from WB2 and the Tichka massif area unit belonged to a mechanically coherent unit that was slightly tilted under compression, the uplifting portion being the Tichka part (Figure 9b). This Late Cretaceous uplift is associated with kilometer-scale erosion associated to early compressive events of the Atlas belt. This is in line with the slight angular unconformity observed on the field between Turonian and Eocene deposits (Froitzheim et al., 1988) (Figure 4d). This also agrees with Domènech et al. (2016) results showing more uplift in the northern part of the eastern MHA than in its southern counterpart at that time.

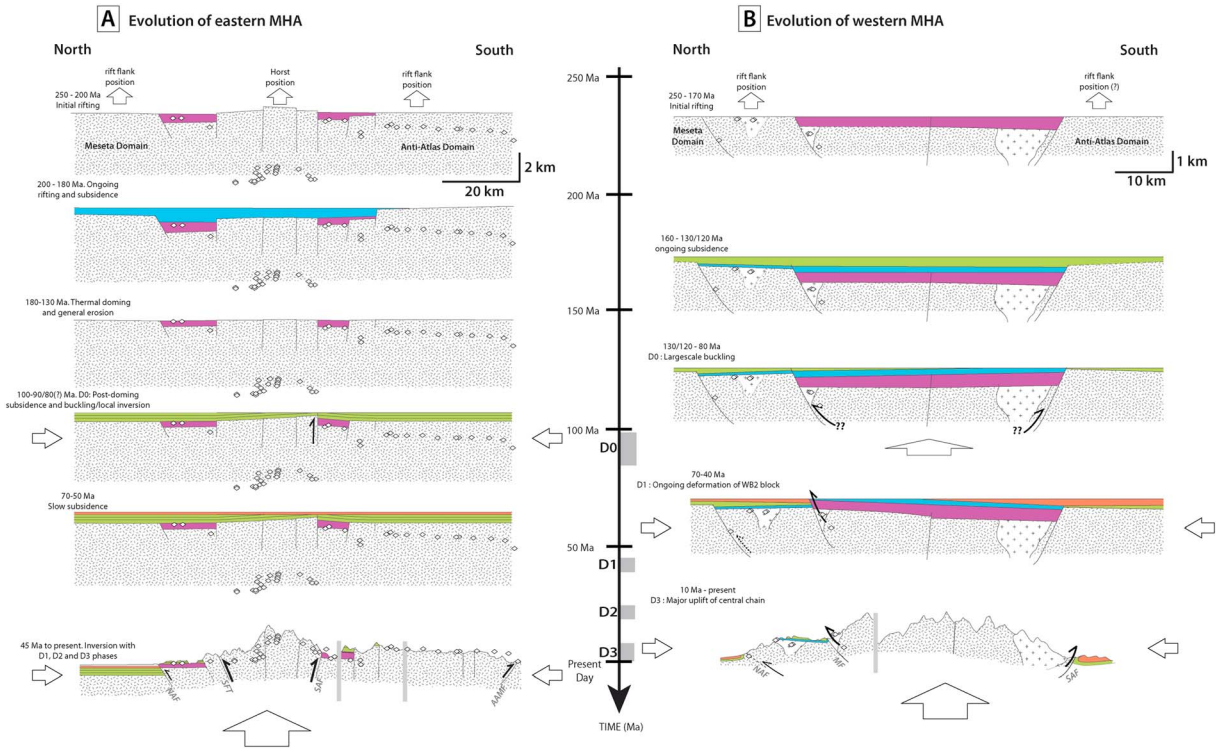

Figure 9. Proposed evolution in cross-section view of the western MHA and the eastern MHA since the Triassic based upon our thermal models. (a) Eastern MHA evolution. (b) Western MHA evolution. The horst geometry is based on Domènech et al. (2016) results on zircon LTT. Small white diamonds locate all the samples that are already given in Figures 3b and 3d. We represent them behaving coherently within each structural unit although some variations in their vertical behavior can exist (details in the text). NAF: North Atlas Front; MF: Medinet Fault; SAF: South Atlas Front; SFT: Sidi Fars Thrust; AAMF: Anti-Atlas Major Fault.

In SF1 unit, the closest samples to the SAF have AFT ages bracketed between 48 ± 3 and 88 ± 5 Ma, whereas farther sample SF1-4 shows a mean AHe age of 74 Ma with an older AFT age (134 ± 3 Ma). Erosion is thus variable during Late Cretaceous with higher amounts close to the SAF (SF1-2/3 samples compared to SF1-4). This event is probably contemporaneous with the erosion occurring in the western MHA. We thus propose that the D0 phase occurred in the beginning of Late Cretaceous given the overall thermal record of the area.

The beginning of Late Cretaceous recorded kilometer-scale uplift, seemingly very localized to faults limiting the inner belt. With our apatite data, it could not be evidenced within the northern foreland but Domènech et al. (2016) were able to evidence it along the northern flank of the MHA, within the inner belt we defined. In the southern foreland, LTT ages distribution advocates for rapid decreasing effects of this event (Figures 3b and 3c). Anyway, Sehrt et al. (2018) got Late Cretaceous-Paleogene AHe ages in the northwestern Anti-Atlas that might be related to this event. Anyway, they did not model the northern samples with these young AHe ages. When modeled, it could properly demonstrate the existence of a wide-scale deformation affecting NW Africa during this period. This first "tectonic" phase is likely related to the onset of the Africa-Europe convergence (Frizon de Lamotte et al., 2009).

5.1.3. Cenozoic Inversion of the MHA

Our results in the inner belt of the eastern MHA show for the first time a three-step Cenozoic evolution, from late Eocene to Quaternary (Figure 8), each step characterizing an uplift phase. The young LTT ages do not give information about the Mesozoic history but allow a robust description of the Cenozoic history. The first erosion phase (D1) occurred between 41 and 35 Ma (Bartonian-Priabonian) with ~3 km of erosion (calculated for a mean geotherm of 30°C km^{-1}). The observation of this late Eocene phase is unique in Morocco, as it was only suspected through facies studies (El Harfi et al., 2001) and attested by few structural observations (Leprêtre, Missenard, Saint-Bezar, et al., 2015). This phase could not be recognized by Domènech et al. (2016) with the use of zircon LTT. They only used some AFT data from Missenard et al. (2008) and Balestrieri et al. (2009) with a debatable approach that consists in putting a time-temperature box

corresponding to the AFT age-annealing zone. They thus cannot consider all the information contained along the belt and select an age range that may be only representative of a portion of the thermal history. Consequently, they propose a major event during the Oligocene-Miocene to account for the data, which is too young compared to the first event we have evidenced here. A second erosion phase (D2) took place in early Miocene (21–17 Ma), with a smaller cooling. This early Miocene phase is associated with the sliding of gravity "nappes" along the SAF in the Ouarzazate foreland basin (Teson & Teixell, 2008; Leprêtre, Missenard, Saint-Bezar, et al., 2015). A third phase (D3) occurred around 10 Ma, with highly variable cooling between samples at different elevations (Figure 8b). This variation is explained by the contemporaneous topographic building. The carving of steep valleys and the building of a strong relief have brought the deeper samples (i.e., at the present-day close to the valleys bottoms) at the surface by larger upward movement than samples at high elevations.

The forelands of the eastern MHA have also recorded the Cenozoic inversion (Figures 7c and 7d). The interpretation of the LTT data is not straightforward, and each unit has differentially recorded the uplift phases. For the samples closest to the fronts (SAF and Sidi Fars Thrust; Figures 2b, 3b, and 3c), AHe ages are the youngest, affected by the motions near the main faults, being in the footwall. They record cooling from Miocene onward, suggesting that uplift has widely affected the belt only since Miocene, being potentially restricted to the inner belt before (Figure 9a).

In the western MHA, phase D1 is recorded in WB2 unit, while WB1 was recording a small subsidence (Figures 7b and 9b). This observation from the earliest times of the orogen building indicates a concentration of the deformation on the Medinet Fault, through unit tilting (Figure 9b). The whole WMHA recorded a final erosion pulse from 10 Ma onward (D3), with the shortening being more distributed. Topography building in this section of the belt seems essentially due to this last uplift phase. This latest massive erosion explains the absence of Upper Cretaceous-Neogene cover in unit WB2 and the Tichka massif area, leaving only scarce Triassic remnants (Figure 2a).

5.2. Characteristics of the Deformation in the MHA

The Cenozoic inversion has concentrated on a narrow zone (~50 km for the western MHA and ~25–30 km for the eastern MHA, Figures 1 and 9) along ~200 km, mostly corresponding to the former Liassic graben. This preferential uplift is recorded between the major faults in the inner belt and the WB2 (and Tichka massif area?) unit (Figures 2a, 7, and 9). Instead, the forelands have only recorded a partial record of the Cenozoic history (Figures 7c and 7d). Some foreland samples have experienced a strong and short heating, which is probably related to their position in the footwall of the major faults since at least the late Eocene (Figure 7c).

5.2.1. How Is the Deformation Focused?

Rheological evolution of a thinned crust during postrift depends on many factors. After rifting, the lithosphere generally cools and can become stronger than the surrounding lithosphere (England, 1983). Young rifts are intuitively weaker given the thermal anomaly supporting the thinned crust, although it crucially depends on the strain rate of the extension, which must be high enough (van Wijk & Cloetingh, 2002). Nonetheless, old rifts can be inverted. For example, a thick sediment cover can act as a thermal blanket (Stephenson et al., 2009) that weakened the lithosphere by heating. At the opposite, weak burial may act on a reverse way (e.g., Lafosse et al., 2016), depending on the strength contrast between the sediments and the basement. Crustal or Moho irregularities may also produce varied heat flows that weaken the rift crust. Lastly, this weakening can stem from the inherited faults that concentrate the stresses (Bonini et al., 2012, and references therein).

In the MHA, the rifting was followed by a minimum interval of 100 Myr before tectonic inversion. This is paradoxical since it should have strengthened the system and impeded its inversion. However, we must notice the following:

1. The crust underlying the Atlas system displays a classical continental crust thickness (Fullea et al., 2010), lower than 40 km. On the contrary, the lithosphere thickness presents anomalously thinned domain under the central High Atlas/MHA, the Middle Atlas, and under the Anti-Atlas, being only 70 km thick in some places.
2. We demonstrate that within the MHA, the rift and postrift sedimentary infills reached kilometric amplitudes and could thus act as a thermal blanket over the former rift zone.

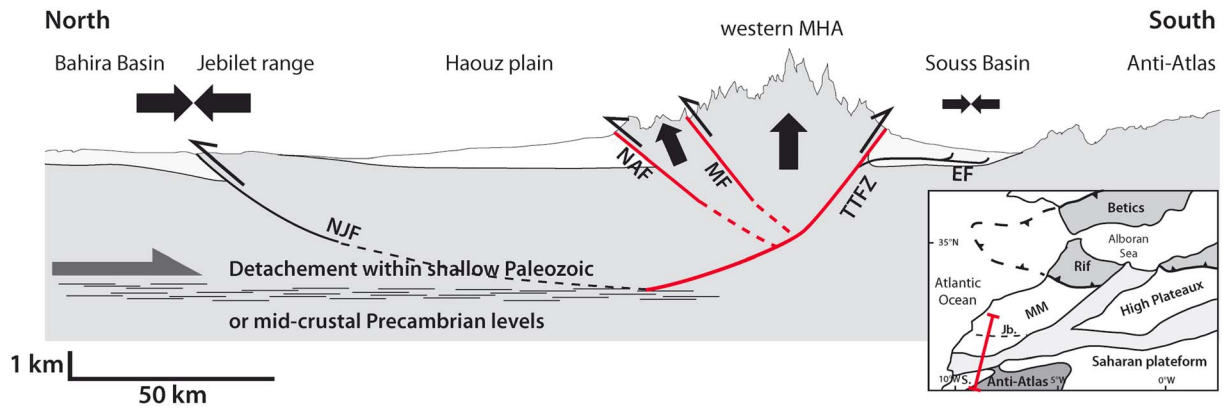

Figure 10. Simple sketch showing the partitioning of deformation between (1) the inner belt where uplift is essentially recorded in contrast with (2) propagating faults in the more or less distal foreland in the Souss Basin (Mustaphi et al., 1997) and the Jebilet range where ~4 km of horizontal shortening is recorded for about 1 km of vertical throw (Hafid et al., 2006). The majority of the shortening is proposed to be transferred to a detachment located within either shallow (Paleozoic?) or a midcrustal (Precambrian?) levels. NJF: North Jebilet Front; NAF: North Atlas Front; MF: Medinet Fault; TTFZ: TiziN'Test Fault Zone; EF: El Kléa Fault. Main post-Paleozoic basins are indicated in clearer grey shade with approximate depths.

3. Last but not least, the Moroccan crust has a long geological history since Precambrian times: for example, the Tizin'Test Fault zone is a Precambrian fault zone and a major lineament that has been active since Panafrican orogeny (Gasquet et al., 2008; Qarbous et al., 2003). It is also thought to branch with crustal décollements involved with the rifting and the recent inversion (El Mustaphi et al., 1997). The importance of the Tizin'Test Fault zone is further confirmed by our results: in the western MHA, it represents the southern front of the belt, along which major inversion has been occurring since the early Cenozoic; in the eastern MHA, it bounds northerly the uplifting unit squeezed between it and the Mesozoic SAF (Figure 2a), which is thought to have a kilometric throw during the Cenozoic inversion (Ghorbal, 2009; Missenard et al., 2007).

In light of these observations, we think that although the postrift phase was long, the inherited crustal weaknesses due to the faults favor at first order the concentration of the stress. Under these circumstances, the thermal weakening due to both the thinned lithosphere and in this case the relatively thick sedimentary cover might have enhanced the inversion process.

5.2.2. Horizontal Versus Vertical Deformation Partionning

Our results demonstrate that erosion has significantly focused on a narrow zone during the Cenozoic inversion. Yet significant displacements have occurred on outer faults. For example, the uplift of the northern unit (with AZ samples) in the western MHA has somehow been important with respect to the Haouz plain (Figure 7b) and this has been controlled by the northern front near Amizmiz and Bozoga (Figure 2a). A southward crustal detachment is also suspected underlying the main anticline structures in the Souss Basin (Figure 2a; Mustaphi et al., 1997), but it did not generate important uplift. It nonetheless sets the deformation front south of the Tizin'Test Fault zone within the Souss Basin. Most importantly, the Jebilet massif north of Marrakech underwent kilometric uplift (Saddiqi et al., 2009) on a north vergent thrust fault accommodating at least 4 km of shortening (Hafid et al., 2006). On a north-south cross section from the north of Jebilet to the SoussBasin (El Kléa Fault, in Mustaphi et al., 1997), based on the LTT data and the literature, we can recognize a structural compartmentalization (Figure 10). On the boundaries of the system, outer faults accommodate mainly horizontal shortening. On the contrary, inner reverse faults accommodate few horizontal shortening, which is transmitted outward on more external thrusts that could likely branch into deeper detachment located into shallow Paleozoic or Precambrian levels.

This kind of deformation partitioning (horizontal shortening on the outer faults and vertical throw along inner faults) demonstrates that during Cenozoic, the MHA behaves like a giant crustal pop-up structure, associating a considerably uplifted core bounded by the former steep rift faults with lateral units moving on less steep thrust faults (like the one north of the Jebilet range). This result illustrates well the thick-skinned nature of the deformation of the MHA, with a deformation guided by basement units moving relatively from one another (Figure 9). Thus, cover deformation is extremely reduced, limited to the moving boundaries

between each unit. In between, the absence of décollement level brings striking evidences for this unit deformation with the conservation of almost undeformed Mesozoic-Cenozoic plateaus in the western MHA (Figure 4c).

5.3. Regional Implications: The MHA in the Atlas Belt

Our LTT study reveals the occurrence of five erosional phases since the rifting stage in Triassic-Early Jurassic times. The first, during the Middle(?)-Late Jurassic/Early Cretaceous, took place during the postrift phase and is likely due to mantle-related phenomenon related to the Atlantic evolution (Leprêtre et al., 2017).

Four compressive steps are then evidenced. The first, in the Late Cretaceous, is heterogeneously recorded and has been observed in the Moroccan offshore (Hafid et al., 2006). This deformation likely records the onset of the Africa-Europe convergence, at the Early-Late Cretaceous transition. This Late Cretaceous deformation has been poorly noticed within the Atlas realm in Algeria, but some subsurface data confirm it in Tunisia (Khomsi et al., 2016, and references therein).

From Cenozoic onward, three deformation phases exist in the MHA. The first phase reaches its climax by the end of late Eocene. It coincides with the Atlasic phase recognized in Algeria and Tunisia (Frizon de Lamotte et al., 2000, for a Maghreb overview; Bracène and Frizon de Lamotte, 2002, for Algeria; and Khomsi et al., 2009, for Tunisia). According to Frizon de Lamotte et al. (2000), this event records the locking of the subduction in the Maghrebian basin before the slab roll-back in western Mediterranean, allowing the intraplate transmission of stresses away from the active margin. The second phase, mainly evidenced in the eastern MHA, is related to the setting of nappes in the MHA and central High Atlas and is confined to Morocco (Leprêtre, Missenard, Saint-Bezar, et al., 2015; Teson & Teixell, 2008). It might be related to a first event of relief building linked with the lithospheric thinning together with minimum compression to trigger the sliding of gravity thrust sheets over the foreland (Leprêtre, Missenard, Saint-Bezar, et al., 2015). Surprisingly, it is not recorded in the western MHA. Following Leprêtre, Missenard, Saint-Bezar, et al. (2015), we argue that it is the setting of these nappes that allows recording this cooling: through an efficient Triassic/Liassic décollement level, they efficiently remove a significant thickness of the upper crust only over the eastern MHA. At last, compression resumed in the late Miocene/early Pliocene with the present-day relief building and important vertical motions within the most inner units of the belt. This phase is widely recorded along the whole Atlas realm (Frizon de Lamotte et al., 2009) related to the Africa-Europe convergence.

As a whole, the Atlas system acts as an efficient proxy that samples the stress state of the lithosphere, in relationship with the convergence processes acting at the active margin boundary. The Miocene additional deformation/erosional stage in the Moroccan High Atlas must be attached to specific lithospheric processes as proposed by Missenard and Cadoux (2012), further confirmed by Kaislaniemi and van Hounen (2014).

6. Conclusion

Using large AFT and AHe data sets across two cross sections of the Marrakech High Atlas, we reconstruct the Mesozoic-Cenozoic evolution of this portion of the High Atlas in Morocco. Through thermal modeling, we were able to demonstrate the occurrence of five erosional events since the Early-Middle Jurassic rifting.

The first erosional event is related to the thermal doming affecting the whole NW Africa at that time. The following events can be linked to the inversion of the rift since Late Cretaceous onward. Our results evidence two periods of inversion. First, a discrete compressional stage occurred during the Late Cretaceous, leaving a slight imprint on the apatite LTT. Second, we show that the three-step Cenozoic inversion is mainly concentrated along the former Jurassic rift boundaries, uplifting the former depocenters. This is permitted through thick-skinned tectonics, particularly showed in the western MHA, where poorly deformed high plateaus are uplifted to more than 1,000 m.

As far as inversion mechanisms are concerned, the LTT pattern clearly identifies a narrow zone concentrating the inversion. Given the length of the postrift stage, that might have strengthened the lithosphere. We propose that the inversion of the former Jurassic rift has been facilitated through (1) the structural rifting inheritance and (2) the thermal lithospheric anomaly that has been emplaced under the MHA since the Miocene. The structure of the MHA is well represented by a giant pop-up structure with most of the vertical uplift concentrated within the axis of the belt, in a complex relationship with the former Mesozoic rift, like in the eastern MHA where the rift geometry was complex.

Acknowledgments
A. Michard is thanked for fruitful discussions on early versions of the manuscript and for sharing his knowledge on the evolution of the western MHA. Data and supporting informations can be found in the following data depository: low-temp-apatite-data-Marrakech-High-Atlas on the website www.github.com.

References

Ayarza, P., Carbonell, R., Teixell, A., Palomeras, I., Martí, D., Kchikach, A., et al. (2014). Crustal thickness and velocity structure across the Moroccan Atlas from long offset wide-angle reflection seismic data: The SIMA experiment. *Geochemistry, Geophysics, Geosystems*, *15*, 1698–1717. https://doi.org/10.1002/2013GC005164

Balestrieri, M. L., Moratti, G., Bigazzi, G., & Algouti, A. (2009). Neogene exhumation of the Marrakech High Atlas (Morocco) recorded by apatite fission-track analysis. *Terra Nova*, *21*(2), 75–82. https://doi.org/10.1111/j.1365-3121.2008.00857.x

Barbarand, J., Carter, A., Wood, I., & Hurford, T. (2003). Compositional and structural control of fission-track annealing in apatite. *Chemical Geology*, *198*, 107–137. https://doi.org/10.1016/S0009-2541(02)00424-2

Beauchamp, W., Allmendinger, R. W., Barazangi, M., Demnati, A., El Alji, M., & Dahmani, M. (1999). Inversion tectonics and the evolution of the High Atlas Mountains, Morocco, based on a geological geophysical transect. *Tectonics*, *18*(2), 163–184. https://doi.org/10.1029/1998TC900015

Bonini, M., Sani, F., & Benedetti, A. (2012). Basin inversion and contractional reactivation of inherited normal faults: A review based on previous and new experimental models. *Tectonophysics*, *522-523*, 55–88. https://doi.org/10.1016/j.tecto.2011.11.014

Bracène, R., & Frizon de Lamotte, D. (2002). The origin of intraplate deformation in the Atlas system of western and central Algeria: From Jurassic rifting to Cenozoic–Quaternary inversion. *Tectonophysics*, *357*(1-4), 207–226. https://doi.org/10.1016/S0040-1951(02)00369-4

Coward, M. (1996). Balancing sections through inverted basins. In P. G. Buchanan & D. A. Nieuwland (Eds.), *Modern developments in structural interpretation, validation and modelling*. *Geological Society Special Publication, 99*, 51–77. https://doi.org/10.1144/GSL.SP.1996.099.01.06

Domènech, M., Teixell, A., Babault, J., & Arboleya, M.-L. (2015). The inverted Triassic rift of the Marrakech High Atlas: A reappraisal of basin geometries and faulting histories. *Tectonophysics*, *663*, 177–191. https://doi.org/10.1016/j.tecto.2015.03.017

Domènech, M., Teixell, A., & Stockli, D. F. (2016). Magnitude of rift-related burial and orogenic contraction in the Marrakech High Atlas revealed by zircon (U-Th)/He thermochronology and thermal modeling. *Tectonics*, *35*, 2609–2635. https://doi.org/10.1002/2016TC004283

El Haimer, F. (2014). Mouvements verticaux post-varisques des domaines mesetiens et atlasique: Thermochronologie bassetempérature sur apatite et zircon (PhD thesis). Casablanca, Morocco: Aïn Chock Sciences faculté, Université Hassan II.

El Harfi, A., Lang, J., Salomon, J., & Chellai, E. H. (2001). Cenozoic sedimentary dynamics of the Ouarzazate foreland basin (Central High Atlas Mountains, Morocco). *International Journal of Earth Sciences*, *90*(2), 393–411. https://doi.org/10.1007/s005310000115

England, P. (1983). Constraints on extension of continental lithosphere. *Journal of Geophysical Research*, *88*(B2), 1145–1152. https://doi.org/10.1029/JB088iB02p01145

Fekkak, A., Ouanaimi, H., Michard, A., Soulaimani, A., Ettachfini, E. M., Berrada, I., et al. (2018). Thick-skinned tectonics in a Late Cretaceous-Neogene intracontinental belt (High Atlas Mountains, Morocco): The flat-ramp fault control on basement shortening and cover folding. *Journal of African Earth Sciences*, *140*, 169–188. https://doi.org/10.1016/j.jafrearsci.2018.01.008

Flowers, R., Ketcham, R. A., Shuster, D., & Farley, K. A. (2009). Apatite (U–Th)/He thermochronology using a radiation damage accumulation and annealing model. *Geochimica et Cosmochimica Acta*, *73*(8), 2347–2365. https://doi.org/10.1016/j.gca.2009.01.015

Frizon de Lamotte, D., Leturym, P., Missenard, Y., Khomsi, S., Ruiz, G., Saddiqi, O., et al. (2009). Mesozoic and Cenozoic vertical movements in the Atlas system. *Tectonophysics*, *475*(1), 9–28. https://doi.org/10.1016/j.tecto.2008.10.024

Frizon de Lamotte, D., Saint-Bezar, B., Bracene, R., & Mercier, E. (2000). The two main steps of Atlas building and geodynamics of the western Mediterranean. *Tectonics*, *19*(4), 740–761. https://doi.org/10.1029/2000T%20C900003

Froitzheim, N., Stets, J., & Wurster, P. (1988). Aspects of Western High Atlas tectonics. In V. H. Jacobshagen (Ed.), *The Atlas System of Morocco*, *Lect. Notes Earth Science* (Vol. 15, pp. 219–244). Berlin: Springer. https://doi.org/10.1007/BFb0011595

Fullea, J., Fernàndez, M., Afonso, J. C., Vergés, J., & Zeyen, H. (2010). The structure and evolution of the lithosphere–asthenosphere boundary beneath the Atlantic-Mediterranean transition region. *Lithos*, *120*(1-2), 74–95. https://doi.org/10.1016/j.lithos.2010.03.003

Galbraith, R. F., & Laslett, G. M. (1993). Statistical models for mixed fission track ages. *Nuclear Tracks and Radiation Measurements*, *21*(4), 459–470. https://doi.org/10.1016/1359-0189(93)90185-C

Gallagher, K. (2012). Transdimensional inverse thermal history modeling for quantitative thermochronology. *Journal of Geophysical Research*, *117*, B02408. https://doi.org/10.1029/2011JB008825

Gallagher, K., Brown, R. W., & Johnson, C. (1998). Fission track analysis and its applications to geological problems. *Annual Review of Earth and Planetary Sciences*, *26*(1), 519–572. https://doi.org/10.1146/annurev.earth.26.1.519

Gasquet, D., Ennih, N., Liegeois, J.-P., Soulaimani, A., & Michard, A. (2008). The Pan-African belt. In A. Michard, et al. (Eds.), *Continental evolution: The geology of Morocco* (Vol. 116, pp. 33–64). Berlin: Springer. https://doi.org/10.1007/978-3-540-77076-3

Gasquet, D., Leterrier, J., Mrini, Z., & Vidal, P. (1992). Petrogenesis of the Hercynian Tichka plutonic complex (Western High Atlas, Morocco): Trace element and Rb-Sr and Sm-Nd isotopic constraints. *Earth and Planetary Science Letters*, *108*(1-3), 29–44. https://doi.org/10.1016/0012-821X(92)90058-4

Gautheron, C., Barbarand, J., Ketcham, R. A., Tassan-Got, L., van der Beek, P., Pagel, M., et al. (2013). Chemical influence on α-recoil damage annealing in apatite: Implications for (U–Th)/He dating. *Chemical Geology*, *351*, 257–267. https://doi.org/10.1016/j.chemgeo.2013.05.027

Gautheron, C., & Tassan-Got, L. (2010). A Monte Carlo approach to diffusion applied to noble gas/helium thermochronology. *Chemical Geology*, *273*, 212–224. https://doi.org/10.1016/j.chemgeo.2010.02.023

Gautheron, C., Tassan-Got, L., Barbarand, J., & Pagel, M. (2009). Effect of alpha-damage annealing on apatite (U-Th)/He thermochronology. *Chemical Geology*, *266*(3-4), 157–170. https://doi.org/10.1016/j.chemgeo.2009.06.001

Ghorbal, B. (2009). Mesozoic to Quaternary thermo-tectonic evolution of Morocco (NW Africa)(PhD thesis). Amsterdam, Netherlands: VrijeUniversiteit.

Ghorbal, B., Bertotti, G., Foeken, J., & Andriessen, P. (2008). Unexpected Jurassic to Neogene vertical movements in "stable" parts of NW Africa revealed by low temperature geochronology. *Terra Nova*, *20*(5), 355–363. https://doi.org/10.1111/j.1365-3121.2008.00828.x

Gleadow, A. J. W., & Duddy, I. R. (1981). A natural long-term track annealing experiment for apatite. *Nuclear Tracks*, *5*(1–2), 169–174. https://doi.org/10.1016/0191-278X(81)90039-1

Görler, K., Helmdach, F. F., Gaemers, P., Heissig, K., Hinsch, W., Mädler, K., et al. (1988). The uplift of the Central High Atlas as deduced from Neogene continental sediments of the Ouarzazate province, Morocco. In V. H. Jacobshagen (Ed.), *The Atlas system of Morocco*, *Lect. Notes Earth Science* (Vol. 15, pp. 361–404). https://doi.org/10.1007/BFb0011601

Hafid, M., Zizi, M., Bally, A. W., & Ait Salem, A. (2006). Structural styles of the western onshore and offshore termination of the High Atlas, Morocco. *Comptesrendus Geosciences*, *338*(1-2), 50–64. https://doi.org/10.1016/j.crte.2005.10.007

Hand, M., & Sandiford, M. (1999). Intraplate deformation in Central Australia, the link between subsidence and faults reactivation. *Tectonophysics*, *305*(1-3), 121–140. https://doi.org/10.1016/S0040-1951(99)00009-8

Hollard, H., & G. Choubert (1985). Carte géologique du Maroc. In *Notes Mém. Serv. Géol. Maroc* (scale 1:1,000,000), 260(2). Royaume du Maroc.
Hurford, A. J. (1990). Standardization of fission track dating calibration: Recommendation by the Fission Track Working Group of the I.U.G.S. Subcommission on geochronology. *Chemical Geology*, *80*(2), 171–178. https://doi.org/10.1016/0168-9622(90)90025-8
Jimenez-Munt, I., Fernàndez, M., Vergés, J., Garcia-Castellanos, D., Fullea, J., Pérez-Gussinyé, M., & Afonso, J. C. (2011). Decoupled crust-mantle accommodation of Africa-Eurasia convergence in the NW Moroccan margin. *Journal of Geophysical Research*, *116*, B08403. https://doi.org/10.1029/2010JB008105
Kaislaniemi, L., & van Hounen, J. (2014). Dynamics of lithospheric thinning and mantle melting by edge-driven convection: Application to Moroccan Atlas mountains. *Geochemistry, Geophysics, Geosystems*, *15*, 3175–3189. https://doi.org/10.1002/2014GC005414
Ketcham, R. A., Gautheron, C., & Tassan-Got, L. (2011). Accounting for long alpha-particle stopping distances in (U–Th–Sm)/He geochronology: refinement of the baseline case. *Geochimica et Cosmochimica Acta*, *75*, 7779–7791. https://doi.org/10.1016/j.gca.2011.10.011
Khomsi, S., Frizon de Lamotte, D., Bedir, M., & Echihi, O. (2016). The Late Eocene and Late iocene fronts of the Atlas Belt in eastern Maghreb: Integration in the geodynamic evolution of the Mediterranean Domain. *Arabian Journal of Geosciences*, *9*, 650. https://doi.org/10.1007/s12517-016-2609-1
Khomsi, S., Ghazi Ben Jamia, M., Frizon de Lamotte, D., Maherssi, C., Echihi, O., & Mezni, R. (2009). An overview of the Late Cretaceous–Eocene positive inversions and Oligo Miocene subsidence events in the foreland of the Tunisian Atlas: Structural style and implications for the tectonic agenda of the Maghrebian Atlas system. *Tectonophysics*, *475*(1), 38–58. https://doi.org/10.1016/j.tecto.2009.02.027
Kraml, M., Pik, R., Rahn, M., Selbekk, R., Carignan, J., & Keller, J. (2006). A new multi-mineral age referencematerial for 40Ar/39Ar, (U-Th)/He and fission track dating methods: The Limberg t3 tuff. *Geostandards and Geoanalytical Research*, *30*(2), 73–86. https://doi.org/10.1111/j.1751-908X.2006.tb00914.x
Kusznir, N. J., & Park, R. G. (1987). The extensional strength of the continental lithosphere: Its dependence on geothermal gradient, and crustal composition and thickness. In M. P. Coward, J. F. Dewey, & P. L. Hancock (Eds.), *Continental extensional tectonics*. *Geological Society of London, Special Publications, 28*, 35–52. https://doi.org/10.1144/GSL.SP.1987.028.01.04
Lafosse, M., Boutoux, A., Bellahsen, N., & Le Pourhiet, L. (2016). Role of tectonic burial and temperature on the inversion of inherited extensional basins during collision. *Geological Magazine*, *153*(5-6), 811–826. https://doi.org/10.1017/S0016756816000510
Laville, E., & Piqué, A. (1991). La distension crustaleatlantiqueetatlasique au Maroc au début du Mésozoïque: Le rejeu des structures hercyniennes. *Bulletin de la SocieteGeologique de France*, *162*(6), 1161–1171.
Leprêtre, R., Missenard, Y., Barbarand, J., Gautheron, C., Pinna-Jamme, R., & Saddiqi, O. (2017). Mesozoic evolution of NWAfrica: Implications for the Central Atlantic Ocean dynamics. *Journal of the Geological Society, London*. https://doi.org/10.1144/jgs2016-100
Leprêtre, R., Missenard, Y., Barbarand, J., Gautheron, C., Saddiqi, O., & Pinna-Jamme, R. (2015). Postrift history of the eastern central Atlantic passive margin: Insights from the Saharan region of South Morocco. *Journal of Geophysical Research: Solid Earth*, *120*, 4645–4666. https://doi.org/10.1002/2014JB011549
Leprêtre, R., Missenard, Y., Saint-Bezar, B., Barbarand, J., Delpech, G., Yans, J., et al. (2015). The three main steps of the Marrakech High Atlas building in Morocco: Structural evidences from the southern foreland, Imini area. *Journal of African Earth Sciences*, *109*, 177–194. https://doi.org/10.1016/j.jafrearsci.2015.05.013
Mattauer, M., Tapponnier, P., & Proust, F. (1977). Sur les mécanismes de formation des chaînesintracontinentales. L'exemple des chaînesatlasiques au Maroc. *Bulletin de la SocieteGeologique de France*, *7*, XIX(3), 521–526.
McDowell, F. W., McIntosh, W. C., & Farley, K. A. (2005). A precise ^{40}Ar–^{39}Ar reference age for the Durango apatite (U–Th)/He and fission-track dating standard. *Chemical Geology*, *214*(3-4), 249–263. https://doi.org/10.1016/j.chemgeo.2004.10.002
Michard, A., Soulaimani, A., Hoepffner, C., Ouanaimi, H., Baidder, L., Rjimati, E. C., & Saddiqi, O. (2010). The south-western branch of the Variscan Belt: Evidence from Morocco. *Tectonophysics*, *492*(1-4), 1–24. https://doi.org/10.1016/j.tecto.2010.05.021
Missenard, Y., & Cadoux, A. (2012). Can Moroccan Atlas lithospheric thinning and volcanism be induced by edge-driven convection? *Terra Nova*, *24*(1), 27–33. https://doi.org/10.1111/j.1365-3121.2011.01033.x
Missenard, Y., Saddiqi, O., Barbarand, J., Ruiz, G. M. H., El Haimer, F., Leturmy, P., & Frizon de Lamotte, D. (2008). Cenozoic thermally induced denudation in the Marrakech High Atlas, Morocco: Insight from fission tracks. *Terra Nova*, *20*(3), 221–228. https://doi.org/10.1111/j.1365-3121.2008.00810.x
Missenard, Y., Taki, Z., Frizon de Lamotte, D., Benammi, M., Hafid, M., Leturmy, P., & Sebrier, M. (2007). Tectonic styles in the Marrakesh High Atlas (Morocco): The role of heritage and mechanical stratigraphy. *Journal of African Earth Sciences*, *48*(4), 247–266. https://doi.org/10.1016/jafrearsci.2007.03.007
Missenard, Y., Zeyen, H., Frizon de Lamotte, D., Leturmy, P., Petit, C., Sébrier, M., & Saddiqi, O. (2006). Crustal versus asthenospheric origin of relief of the Atlas Mountains of Morocco. *Journal of Geophysical Research*, *111*, B03401. https://doi.org/10.1029/2005JB003708
Mrini, Z., Rafi, A., Duthou, J.-L., & Vidal, P. (1992). Chronologie Rb-Sr des granitoïdes hercyniens du Maroc: Conséquences. *Bulletin de la SocieteGeologique de France*, *163*(3), 281–291.
Mustaphi, H., Medina, F., Jabour, H., & Hoepffner, C. (1997). Le bassin du Souss (zone de faille du Tizin'Test, Haut Atlas occidental, Maroc): Résultatd'une inversion tectoniquecontrôlée par une faille de détachementprofonde. *Journal of African Earth Sciences*, *24*(1-2), 153–168. https://doi.org/10.1016/S0899-5362(97)00033-X
Petit, J.-P. (1976). La zone de décrochements du TziN'Test (Maroc) et son fonctionnement depuis le carbonifère (PhD thesis). Université des sciences et techniques de Montpellier 2.
Proust, F., Petit, J.-P., & Tapponnier, P. (1977). L'accident du Tizin'Testet le rôle des décrochements dans la tectonique du Haut Atlas occidental (Maroc). *Bulletin de la SocieteGeologique de France*, *7*(XIX), 541–551.
Qarbous, A., Medina, F., Hoepffner, C., M'fedalAhmamou, M., Errami, A., & Bensahal, A. (2003). La chronologie du fonctionnement de la zone de failles de Tizin'Test: Apport de l'étude des bassinsstéphano-autuniens et permo-triasiques du Haut Atlas occidental (Maroc). *Bulletin de l'InstitutScientifique, Rabat*, *25*, 43–53.
Recanati, A., Gautheron, C., Barbarand, J., Missenard, Y., Pinna-Jammes, R., Tassan-Got, L., et al. (2017). Helium trapping in apatite damage: Insights from (U-Th-Sm)/He dating of different granitoid lithologies. *Chemical Geology*, *470*, 116–131. https://doi.org/10.1016/j.chemgeo.2017.09.002
Saddiqi, O., El Haïmer, F., Michard, A., Barbarand, J., Ruiz, G. M. H., Mansour, E. M., et al. (2009). Apatite fission-track analyses on basement granites from south-western Meseta, Morocco: Paleogeographic implications and interpretation of AFT age discrepancies. *Tectonophysics*, *475*(1), 29–37. https://doi.org/10.1016/j.tecto.2009.01.007
Sandiford, M. (1999). Mechanics of basin inversion. *Tectonophysics*, *305*(1-3), 109–120. https://doi.org/10.1016/S0040-1951(99)00023-2
Sehrt, M., Glasmacher, U. A., Stockli, D. F., Jabour, H., & Kluth, O. (2018). The southern Moroccan passive continental margin: An example of differentiated long-term landscape evolution in Gondwana. *Gondwana Research*, *53*, 129–144. https://doi.org/10.1016/j.gr.2017.03.013

Sinan, M. (2000). Méthodologie d'identification, d'évaluationet de protection des ressourcesen eau des aquifères régionaux par la combinaison des SIG, de la géophysique et de la géostatistique: Application à l'aquifère du Haouz de Marrakech (Maroc). Application à l'aquifère du Haouz de Marrakech (Maroc) (PhD thesis). Rabat, Morocco: Université Mohamed V.

Stephenson, R., Egholm, D. L., Nielsen, S. B., & Stovba, S. M. (2009). Role of thermal refraction in localizing intraplate deformation in southeastern Ukraine. *Nature Geoscience*, *2*(4), 290–293. https://doi.org/10.1038/NGEO479

Teixell, A., Ayarza, P., Zeyen, H., Fernandez, M., Arboleya, M.-L. (2005). Effects of mantle upwelling in a compressional setting: The Atlas Mountains of Morocco. *Terra Nova*, *17*(5), 456–461. https://doi.org/10.1111/j.1365-3121.2005.00633.x

Teson, E., & Teixell, A. (2008). Sequence of thrusting and syntectonic sedimentation in the eastern thrust belt (Dadès and Mgoun Valleys, Morocco). *International Journal of Earth Sciences*, *97*(1), 103–113. https://doi.org/10.1007/s00531-006-0151-1

van Wijk, J. W., & Cloetingh, S. A. P. L. (2002). Basin migration caused by slow lithospheric extension. *Earth and Planetary Science Letters*, *198*(3–4), 275–288. https://doi.org/10.1016/S0012-821X(02)00560-5

Ziegler, P. A., Cloetingh, S., & van Wees, J. D. (1995). Dynamics of intra-plate compressional deformation: The Alpine foreland and other examples. *Tectonophysics*, *252*(1-4), 7–59. https://doi.org/10.1016/0040-1951(95)00102-6